

Supplementary Materials for

Rapid Folding of DNA into Nanoscale Shapes at Constant Temperature

Jean-Philippe J. Sobczak, Thomas G. Martin, Thomas Gerling, Hendrik Dietz*

*To whom correspondence should be addressed. E-mail: dietz@tum.de

Published 14 December 2012, *Science* **338**, 1458 (2012)

DOI: 10.1126/science.1229919

This PDF file includes:

Materials and Methods

Supplementary Text

Figs. S1 to S34

Full Reference List

Other Supplementary Material for this manuscript includes the following:

(available at www.sciencemag.org/cgi/content/full/338/6113/1458/DC1)

Tables S1 to S17 (as a zipped archive):

Table S1 platelike object sequences

Table S2 bricklike object sequences

Table S3 gearlike sequences

Table S4 hinged-bar object sequences

Table S5 bricklike object sequence permutation 1 sequences

Table S6 bricklike object sequence permutation 2 sequences

Table S7 bricklike object with mismatches sequences

Table S8 bricklike object long staple strands sequences

Table S9 bricklike object moderate bend sequences

Table S10 bricklike object strong bend sequences

Table S11 bricklike object strand breaking variation A sequences

Table S12 bricklike object strand breaking variation B sequences

Table S13 bricklike object strand breaking variation C sequences

Table S14 bricklike object strand breaking variation D sequences

Table S15 bricklike object strand breaking variation E sequences

Table S16 bricklike object strand breaking variation F sequences

Table S17 single-layer rectangle sequences

All questions about this material should be directed to the authors.

Materials and Methods

Materials

DNA scaffold strands were prepared as previously described (5). DNA staple oligonucleotide strands were prepared by solid-phase chemical synthesis (Eurofins MWG, Ebersberg, Germany) with Eurofins MWG HPSF (for objects) or HPLC purification grade (for hairpin DNA strands). SYBR Green (SG) nucleic acid stain and ‘ultra-pure’-grade agarose for electrophoresis was purchased from Life Technologies. SG was stored in aliquots at -20°C. Uranyl formate for negative staining was purchased from SPI. All other reagents including buffers, salts, etc were purchased either from Carl Roth or Sigma Aldrich. Heating and cooling of reaction mixtures for shock-freezing experiments were carried out using TETRAD (MJ Research, now Biorad) thermal cycling devices. Fluorometrically-monitored heating and cooling of reaction mixtures were carried out using two identically configured MX3005P RT-PCR devices (Agilent). TEM imaging was performed using a Philips CM100 transmission electron microscope operated at 100 kV. Images were recorded with an AMT 4x4 Megapixel CCD camera. Ethidium-bromide stained agarose gels were scanned using a Typhoon 9500 FLA laser scanner (GE Healthcare). Mathematica (Wolfram Research) was used to transform laser-scanned greyscale gel photographs into 3D landscape images for better appreciation of intensity differences. Igor Pro (Wavemetrics) was used to process fluorometric data.

Cryogenic reaction quench

Assembly reactions were prepared using a 10x folding buffer that gave 1x solutions containing 5 mM TRIS, 1 mM EDTA, 5 mM sodium chloride at pH 8. 20 mM magnesium chloride, 20 nM scaffold DNA, and 200 nM of each staple DNA strand were added, if not otherwise noted. For assembly of the single-layer rectangle object, 12 mM magnesium chloride, 10 nM scaffold DNA and 100 nM of each staple DNA strand were added. Reactions were aliquoted into a suitable number of PCR strip tubes to give a set of identical reactions in separate vessels with 50 µl volume each. The vessels were subjected in parallel to a desired thermal ramping protocol. As the protocol proceeded, individual reaction vessels were rapidly extracted from the thermal cycling apparatus at desired time points or temperatures and immediately immersed into liquid nitrogen for shock freezing. After completion of the entire thermal ramping protocol, all samples were quickly thawed (timescale ~ 3 minutes) and either electrophoresed on 2% agarose gels stained with ethidium bromide and 11 mM MgCl₂ in an ice-water bath or further processed for TEM imaging.

Fluorometric assay

Full object assembly reactions containing scaffold and staple DNA as described above were supplemented with 160 nM SG (if not otherwise noted), resulting in a stoichiometry of 1 SG molecule per ~900 DNA basepairs if all scaffold bases would form basepairs, which ensures negligible influence on DNA hybridization processes. 50 µl reaction volumes were aliquoted each into typically eight PCR strip tubes. In addition, reference reactions were prepared where either the scaffold or staple DNA component was omitted and replaced by water. Another set of reference reactions consisted in

solutions containing folding buffer and a thermally stable DNA hairpin (melting point at ~95°C) with a 23 basepair long stem of sequence



that was used to mimic a solution with a temperature-independent content of DNA basepairs. Monitoring the hairpin reference reaction helped separating factors that influence the measured fluorescence intensity of SG that are intrinsic to SG and to the binding between SG and DNA basepairs from those stemming from actual changes in the solution content of DNA basepairs. It was also useful for comparing signals obtained from the two RT-PCR devices used for this study. All reactions (typically 32 per thermal ramping experiment, consisting in 8x full reaction, 8x staple-only reaction, 8x hairpin-only reaction, 8x 1x buffer-only reaction) were placed in the RT-PCR thermal cycling apparatus and subjected in parallel to a preprogrammed thermal ramping protocol, where the SG fluorescence intensity was read out in a sample-per-sample fashion at specified time-points using a robotic arm equipped with fiber optics for fluorescence measurements.

The typical data obtained and the strategy used for their analysis is outlined in Supporting Figure S1 in which data from a typical cooling experiment from 65°C down to 25°C is shown (that is, a reaction that spent 5 min at 65°C, followed by stepwise cooling to 60°C with a rate of 1 K per 15 min, followed by stepwise cooling with a rate of 1 K per 3h). The data consisted in a list of fluorescence intensity measurements (averaged from the measurements obtained from samples of the same kind) that may be plotted as intensity over time (Fig. S1A) or over temperature (Fig. S1B). Overall, the fluorescence intensity increased as the temperature was lowered for all samples. The hairpin reaction featured a constant, temperature-independent DNA basepair concentration. The increasing fluorescence intensity in the hairpin reaction upon cooling is due to an increasing affinity of SG for DNA for decreasing temperature, and a temperature-dependent fluorescence brightness of SG. The hairpin data could be quantitatively described using a bimolecular reaction scheme for the binding of SG to DNA basepairs and a quadratic fluorescence brightness increase as the temperature is lowered. Note that the stepwise cooling executed by the apparatus manifested itself in step-wise increases in the fluorescence intensity of the hairpin reaction, reflecting that SG binding to DNA equilibrated faster than the period at which intensity measurements were taken (one per 5 minutes in thermal ramping experiments for figure 1 and 2, and one per 30 seconds for kinetic studies for Figure 3).

The signals obtained from the scaffold-only, staple-only, and full object reactions each featured a unique time- and temperature dependent behavior. The data obtained from the scaffold-only reaction suggested that the scaffold strand formed significant secondary structure elements upon cooling from 60°C down to 40°C. For temperatures below 40°C, the signal obtained from the scaffold reaction ran largely in parallel to the hairpin reaction, reflecting that no additional basepairs were being formed. By contrast, the intensity signal of the staple-only reaction featured a steeper slope over the entire temperature range shown than the hairpin reference reaction. Thus, in the staple-only reaction basepairs were formed in the entire range from 60°C down to 25°C.

In the example given in Fig S1, the signal obtained from the full object reaction bore similarities to those obtained from the staple-only reaction but differed noticeably in the temperature range between 59°C and 54°C (i.e within the first 35 hours of the thermal ramping experiment) (Fig. S1C). In particular, in the full object reaction some incubation steps featured pronounced saturation-type fluorescence increases (Fig. S1C) that were not observed in the other reactions and that reflected the formation of object-related DNA basepairs. By computing the fluorescence intensity change $\Delta(t, T)$ upon incubation for time t at temperature T as depicted in figure S1C, a temperature-dependent measure for object formation (Fig. S1D, dashed line) was obtained. This signal was corrected for contributions from staple-background DNA-basepair formation by subtracting the change in fluorescence intensity observed in the staple-only reference reaction. This procedure resulted in what is denoted as the ‘rate-of-folding’ data in the main text (Fig. S1D, solid line).

Unfolding studies were performed analogously, but all objects were first folded and then denatured by heating. For the unfolding results in figure 1, the DNA plates, bricks, and gears were folded using optimal-temperature folding, while the data for hinged-bar and DNA brick versions in figure 2 was acquired after stepwise cooling.

Note that when incubating SG with DNA at higher temperatures, the fluorescence intensity of the sample first increased over several hours, even when changes in the DNA basepair content could be ruled out (Fig. S2A). The phenomenon did also occur when subjecting DNA-free SG solutions to higher temperatures and adding DNA later. Contributions from the apparatus used for the measurements could be ruled out. We speculate that the phenomenon may reflect a type of DNA-dependent chemical activation of SG. To avoid compromising data integrity regarding the formation of DNA basepairs as measured by the fluorescence intensity of SG, all fluorometric measurements included a sufficiently long initial incubation period to obtain stable and reproducible fluorescence intensity measurements (Fig. S2C).

Supplementary Text

Tile-based DNA Objects

The DNA strands for the set of experiments described herein were kindly provided by Bryan Wei and Peng Yin (Wyss Institute, Harvard University). Self-assembly reaction mixtures were prepared as previously described (14). In one set of experiments, the folding of objects denoted as ‘R6’ and ‘R7’ (14) was investigated fluorometrically as described in the Materials and Methods section. In contrast to templated DNA self-assembly, no background correction by subtracting signals from staple-only reaction mixtures could be employed, since the objects consisted only of staple strands. The rate-of-folding trace observed for the object R6 upon cooling featured a peak centered at 53°C (Fig. S3A, solid line). A previously used thermal ramp (14) gave similar results (Fig. S3A, dashed line). For the object R7, the rate of folding featured a less distinct peak as compared to the object R6 that was centered at 50°C (Fig. S3B). Upon re-heating the reaction mixture for object R7, the observed rate of unfolding trace featured a peak shifted toward higher temperatures as compared to cooling. Note that for both objects the

lower temperature boundary of the peak in the rate of folding trace was less distinct than in data obtained for templated objects.

In another set of experiments, ‘R6’ assembly reaction mixtures were incubated for 3h at 47°C, and another at 39°C, while ‘R7’ assembly reaction mixtures were incubated for 3h at either 45°C or 40°C. These temperatures sampled candidates for the lower temperature peak boundary in the rate of folding data. All reaction mixtures were incubated for 10 minutes at denaturing 90°C before initiating thermal ramping. Reactions products were compared electrophoretically to products obtained using a previously reported protocol (14) (Fig. S3C). A broad smear was observed in all reactions that extended from the gel pocket to the leading band that reflected the pool of non-incorporated source strands. Faint but distinct bands were observed in lanes in which products from the ‘R6’ reaction mixture that was exposed to 3h incubation at 47°C, products from the ‘R7’ reaction that was exposed to 3h incubation at 45°C, and products from the respective annealing-based protocols (14) were run. An additional assembly reaction mixture for ‘R6’ was set up that was subjected to stepwise cooling through the peak range of the rate of folding data given in figure S1A, that is from 54°C to 49°C at a rate of 1°C per 1 hour. This reaction yielded a comparably intense target product band. The yield of monomers is approximately 2-fold higher using the peak-sampling protocol and the higher molecular weight smear is less intense than in the control reaction (14). Note that this is achieved in 1/3 of the previously necessary reaction time.

The above suggest that the fluorometric assay is also applicable to study the folding and unfolding of tile-based DNA objects. Note that the assay may be less precise than for templated DNA objects owing to a lack of suitable reference reactions. The comparatively broad peaks observed in the rate of folding data suggest that the fundamental assembly mechanism for tile-based objects may be less cooperative than for objects that form on a long template strand. The assembly of tile-based objects may thus require some degree of thermal ramping.

Gel Electrophoresis Data

Gel image data depicted in the main text was transformed from 2D greyscale-format to 3D landscape mode for better appreciation of absolute intensities and intensity differences. To this end, Mathematica (Wolfram Research) was employed using the exemplary code given below.

```
gelTyp = ImageData[ drag & drop image data here ];
gelTypTrans = Transpose[gelTyp];
a2 = 0.2;
b2 = 1 - Min[gelTypTrans[[px_x1 ;; px_x2, px_y1* ;; px_y2]]] //scaled ROI
multGel2 = 1/b2
multColor2 = (1 - a2)
ListPlot3D[multGel2*(1 - gelTypTrans[[px_x1 ;; px_x2, px_y1 ;; px_x2]]),
MaxPlotPoints -> 500, PlotRange -> {0, 1}, Boxed -> False, Axes -> None,
ColorFunction ->
Function[{x, y, z}, ColorData["Rainbow"][[z*multColor2 + a2]]],
ColorFunctionScaling -> True, BoxRatios -> {2, 3.236, 0.5},
ViewPoint -> {0.00001, 0, 3}, ImageSize -> 1000, Mesh -> None]
```

In Figures S4-S6, source images of all gel electrophoresis data shown in the main manuscript and Fig. S8 are provided, including also marker and template reference lanes. The labels ‘T’ and ‘M’ denote template strands and 1kb marker lanes, respectively. The label ‘#’ (gels for figure 3 and S8, time-resolved folding) denotes reactions denatured for 15 min at 65°C, followed by extraction and shock-freezing right before the thermal cycling apparatus had started cooling to the target temperature. Lanes labeled with ‘0-minute incubation’, by contrast, refer to samples that were extracted and shock-frozen right after the thermal cycling apparatus had reached the target temperature. Lanes labeled with ‘C’ were control reaction mixtures containing folded objects. Lanes labeled with ‘7d’ refer to products from reaction mixtures exposed to 173 hours long control thermal annealing as in (8).

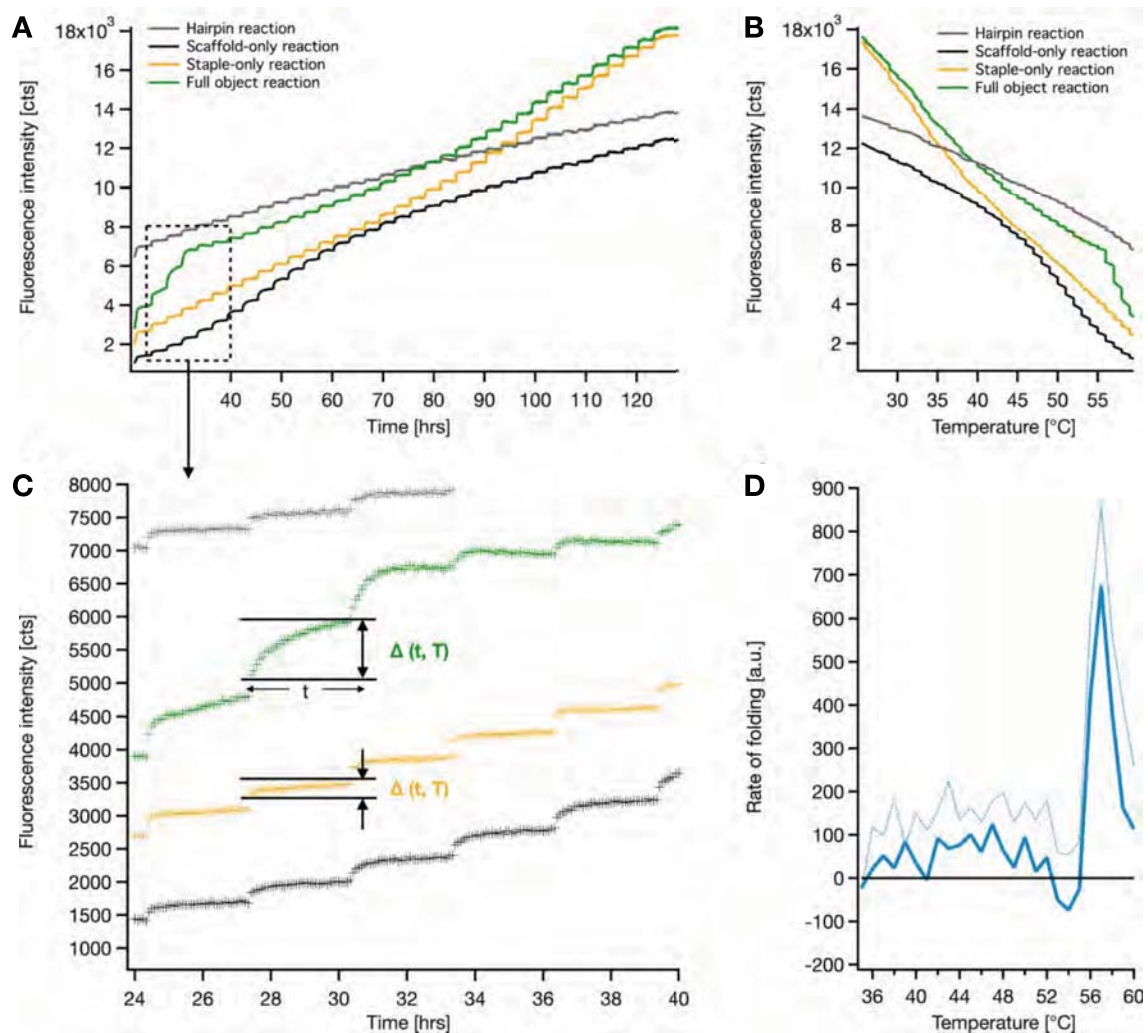


Fig. S1

Fluorometric data and data processing. See section Materials and Methods/Fluorometric Assay for a detailed description. (A) Fluorescence intensity versus time obtained for stepwise heating of reaction mixtures containing scaffold and staple DNA strands (“Full object reaction”), either scaffold or staple DNA strands (“Scaffold-only reaction”, “Staple-only reaction”, respectively), or a stable DNA hairpin (“Hairpin reaction”). (B) The same signals, but plotted as a function of the temperature at each point in time were measurements were taken. (C) Zoom into (A). (D) Rate of folding versus temperature after subtracting the increase in fluorescence obtained after incubation for time t at temperature T in the staple only reaction from the corresponding increase observed in the full object reaction.

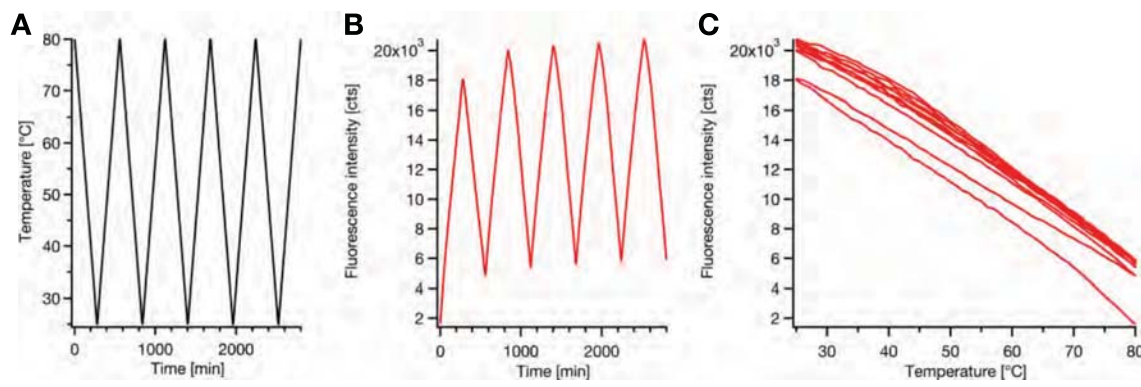


Fig. S2

SYBR Green fluorescence creep. **(A)** A reaction mixture containing a temperature-independent DNA basepair concentration of ~40 μ M (as realized by thermally stable DNA hairpin) and containing 120 nM SG was subjected to the temperature ramping protocol shown. **(B)** Evolution of the fluorescence intensity recorded during execution of the protocol in (A). The signal reveals slow creep toward greater intensities. The signal creep disappears after ~1500 minutes of thermal ramping. **(C)** Same data as in (B), but plotted as intensity over temperature to visualize that the signal becomes stable and reproducible after sufficient thermal cycles. The signal creep could also be eliminated by 20-hour-long incubation at 60°C, or 10-hour-long incubation at 70°C.

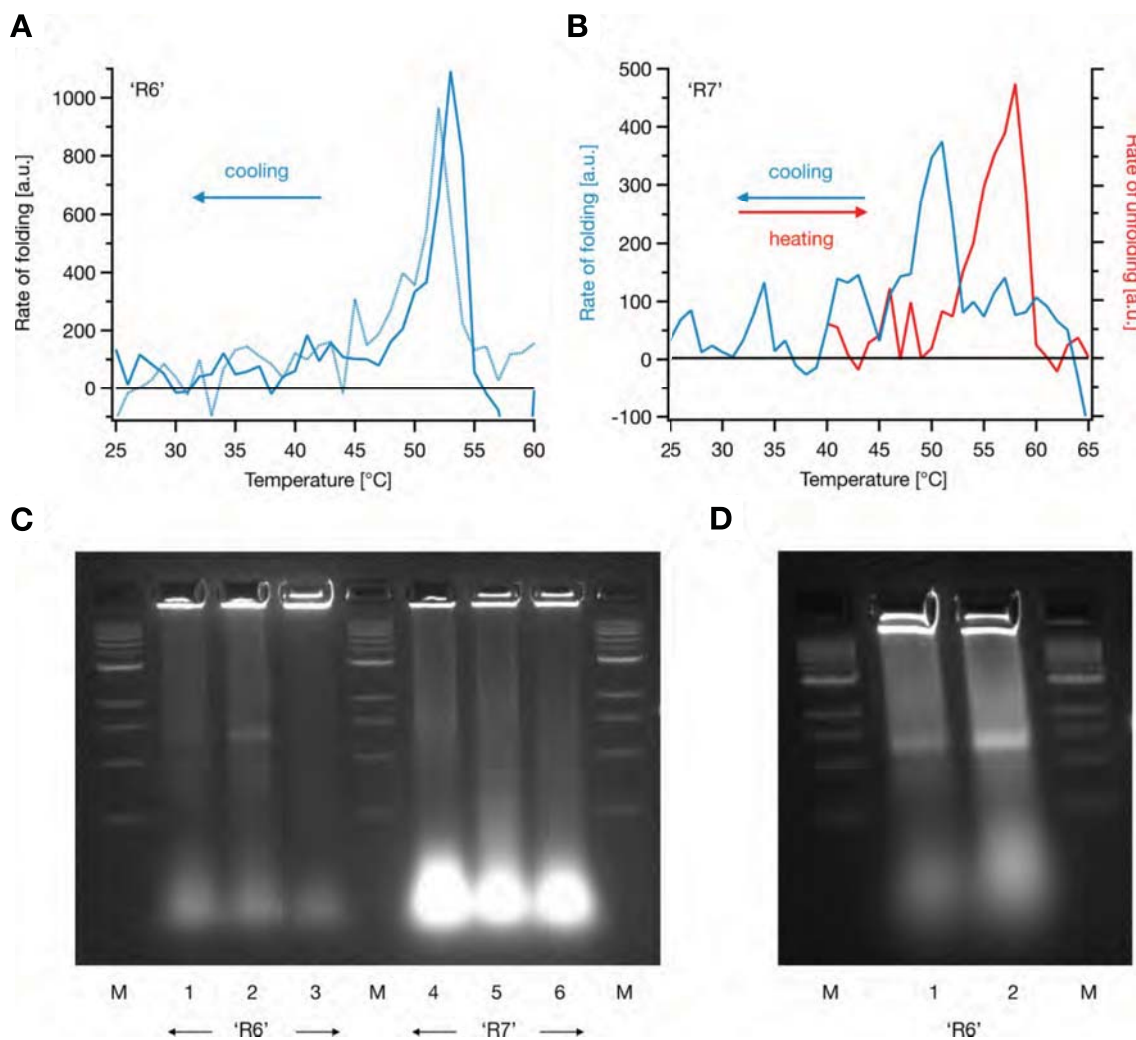


Fig. S3

Tile-based DNA objects. **(A)** Fluorometric rate of folding obtained for object 'R6' from (14) Solid line: step-wise cooling using 3h incubation per degree Celsius. Dashed line: results obtained using a previously reported thermal annealing ramp (14). **(B)** Cooling and heating a self-assembly reaction mixture for object 'R7' (14) using step-wise cooling with 3h incubation per degree Celsius. **(C)** Photograph of a Ethidium-Bromide stained 2% agarose gel. M = 1kB marker. 1 = incubation of R6 reaction mixture at 47°C for 3h; 2= Wei et al assembly conditions; 3 = incubation of R6 reaction mixture at 39°C for 3h; 4 = incubation of R7 reaction mixture at 45°C for 3h; 5= Wei et al assembly conditions (14); 6 = incubation of R7 reaction at 40°C for 3h. **(D)** Photograph of a Ethidium-Bromide stained 2% agarose gel. M = 1kB marker. 1 = 'R6' folded with Wei et al assembly conditions (14); 2 = step-wise cooling of R6 reaction mixture from 54°C to 49°C with a rate of 1°C per 1 hour. All reactions were heated to 90° for 10 minutes before starting the thermal ramping. See also section "Tile-based objects" in the Supplementary Text.

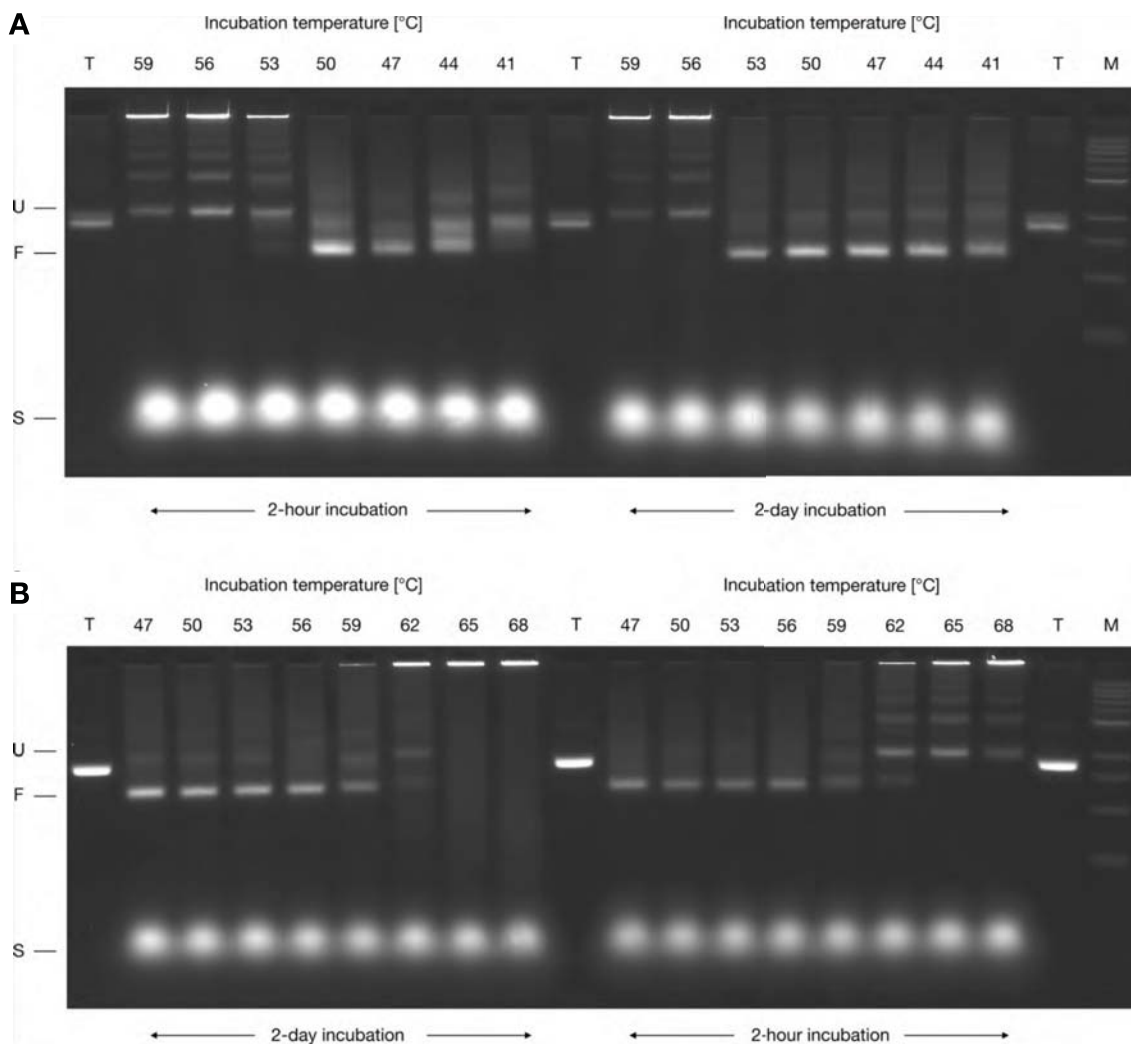


Fig. S4

Long-term constant temperature incubation of brick-like objects. (A) Photograph of a ethidium-bromide stained 2% agarose gel on which products from assembly reactions were electrophoresed. T = template strands. U = unfolded objects. F = folded objects. S = excess staple strands. Assembly reaction mixtures for brick-like DNA objects were first exposed to denaturing temperatures by heating to 65°C for 15 minutes, followed by a temperature jump to a defined set of lower temperatures where the mixtures were then incubated for either 2 hours or 2 days. For two-hour long incubation, quickly migrating, folded objects (marked with the letter 'F') appeared in the reaction mixtures that have been incubated at 50°C and 47°C (faintly present also in the 53°C reaction). By contrast, for two-day long incubation, the reaction mixture incubated at 53°C now contained predominantly folded objects. Also, products in the reaction mixtures that were incubated at 47°C down to 41°C contained products with higher mobility as compared to the two-hour long incubation. The fact that the nature of the reaction products depended on incubation timescale showed thus that the folding process was not in equilibrium. (B) Photograph of a ethidium-bromide stained 2% agarose gel on which products from assembly reactions were electrophoresed. Reaction mixtures containing previously folded

objects (through 3-hour incubation at 47°C) were heated and incubated at a defined set of higher temperatures for either 2 days or 2 hours. The observed pattern of reaction products did not differ between the two-day versus two-hour long incubation, except for a more pronounced smear in the lanes for 2 day incubation at temperatures above 59°C, which points to material degradation. These findings and time-resolved results reported in figure 3 showed that unfolding occurred rapidly and the temperature dependence of the results obtained did not depend on the timescale of the unfolding experiments.

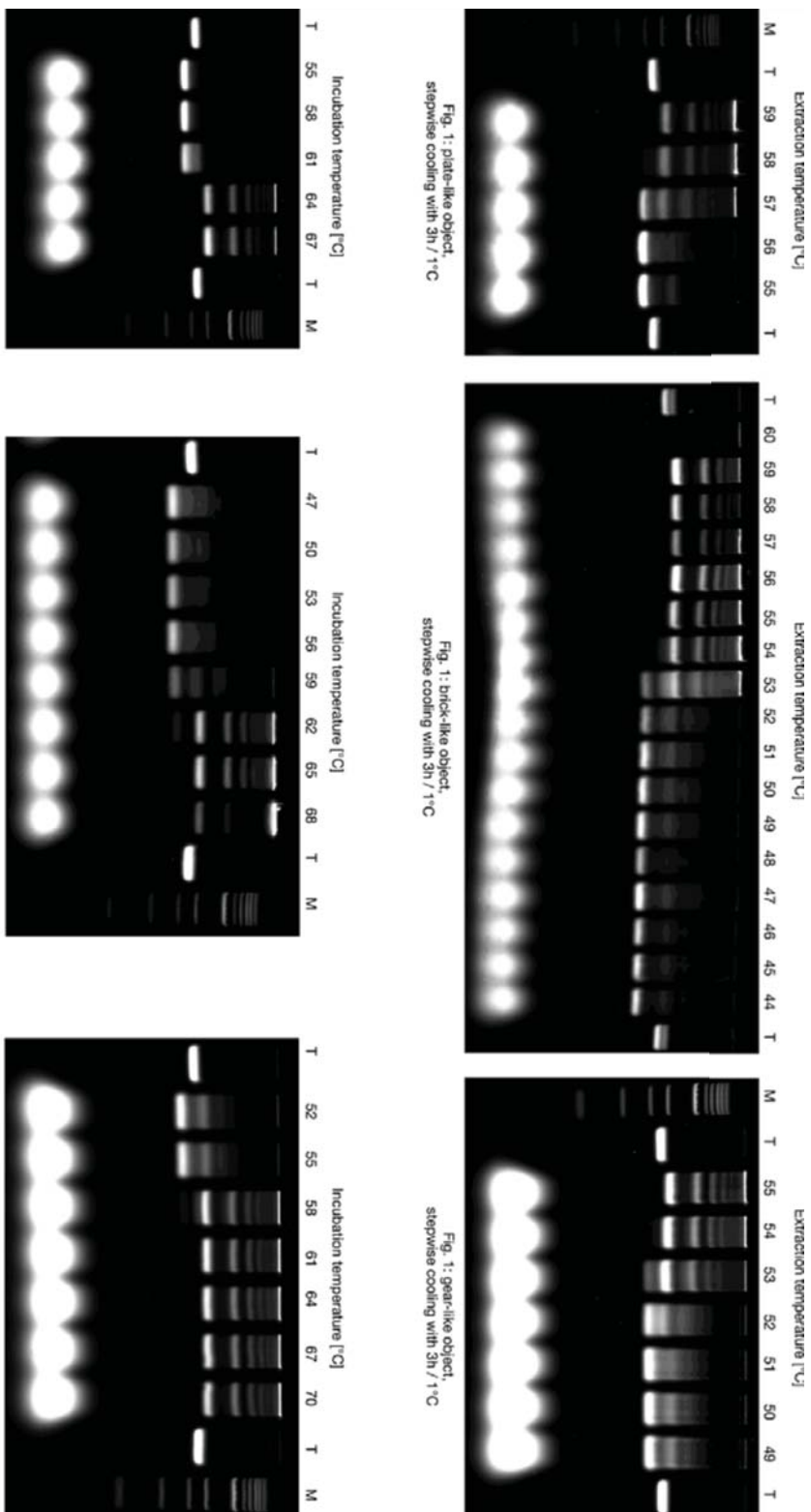


Fig. 1: plate-like object,
2h heat-denaturation

Fig. 1: brick-like object*,
stepwise cooling with 3h / 1°C

Fig. 1: gear-like object,
stepwise cooling with 3h / 1°C

Fig. 1: gear-like object*,
2h heat-denaturation

Fig. S5

Source gel photographs for 3D landscape images in Figure 1.

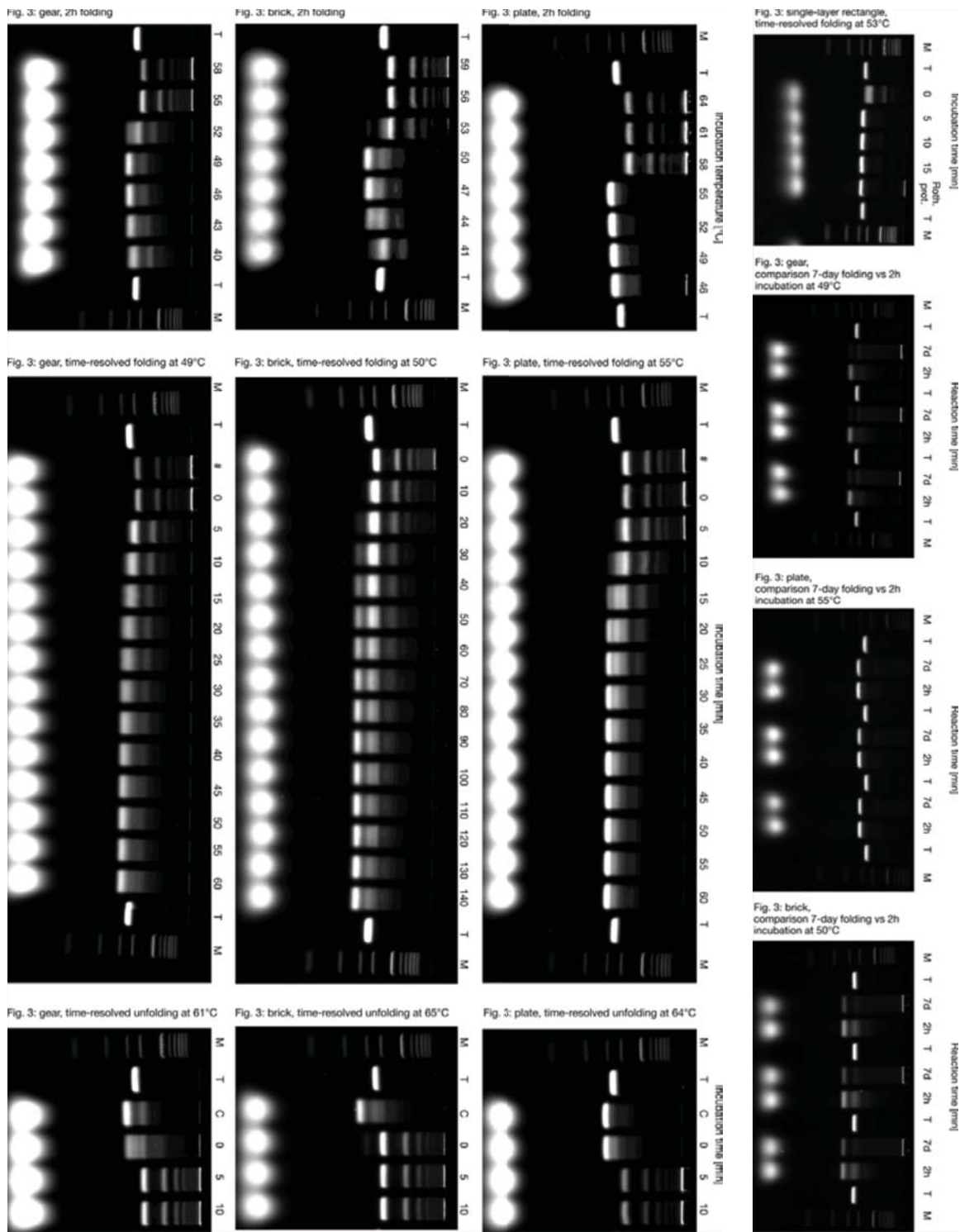


Fig. S6

Source gel data for Figure 3 and Figure S8.

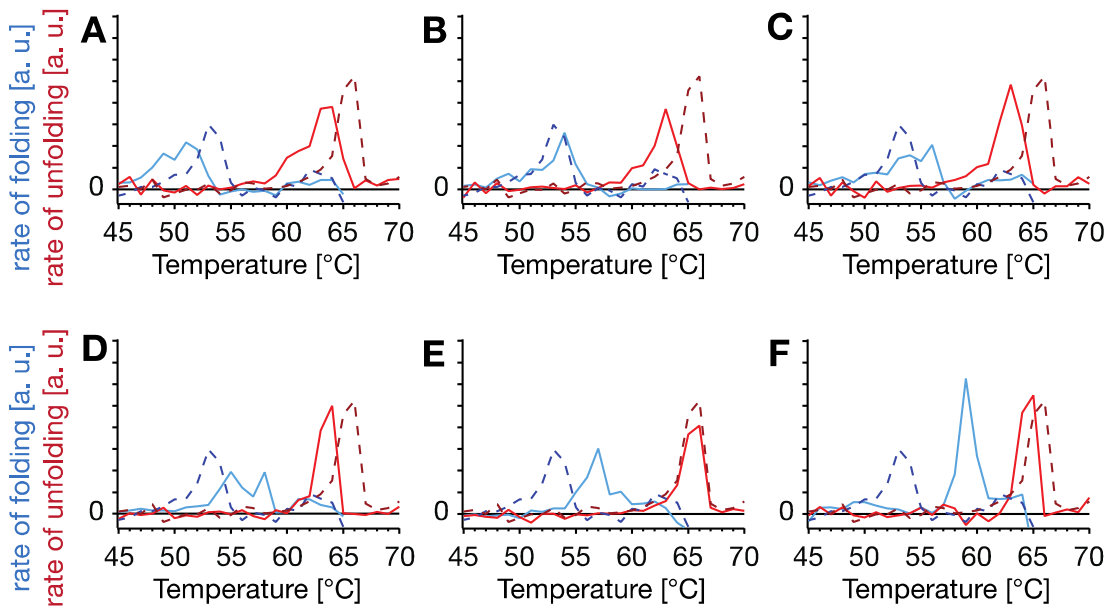


Fig. S7

Influence of staple strand routing on folding and unfolding behaviour. Fluorometric rate of folding (blue line) upon stepwise cooling and rate of unfolding (red line) upon stepwise heating reaction mixtures for six variants of the brick-like 3D DNA object. See also Fig. 2. Dashed line gives signals obtained for the ‘default’ version of the brick-like object shown in Figure 1. Variants were achieved by staple strand routing and breakpoint position variations, but used identical template routing and template sequence permutation. The version for (F) featured an overall reduced staple strand crossover density. Supporting figures S28-S33 show design details.

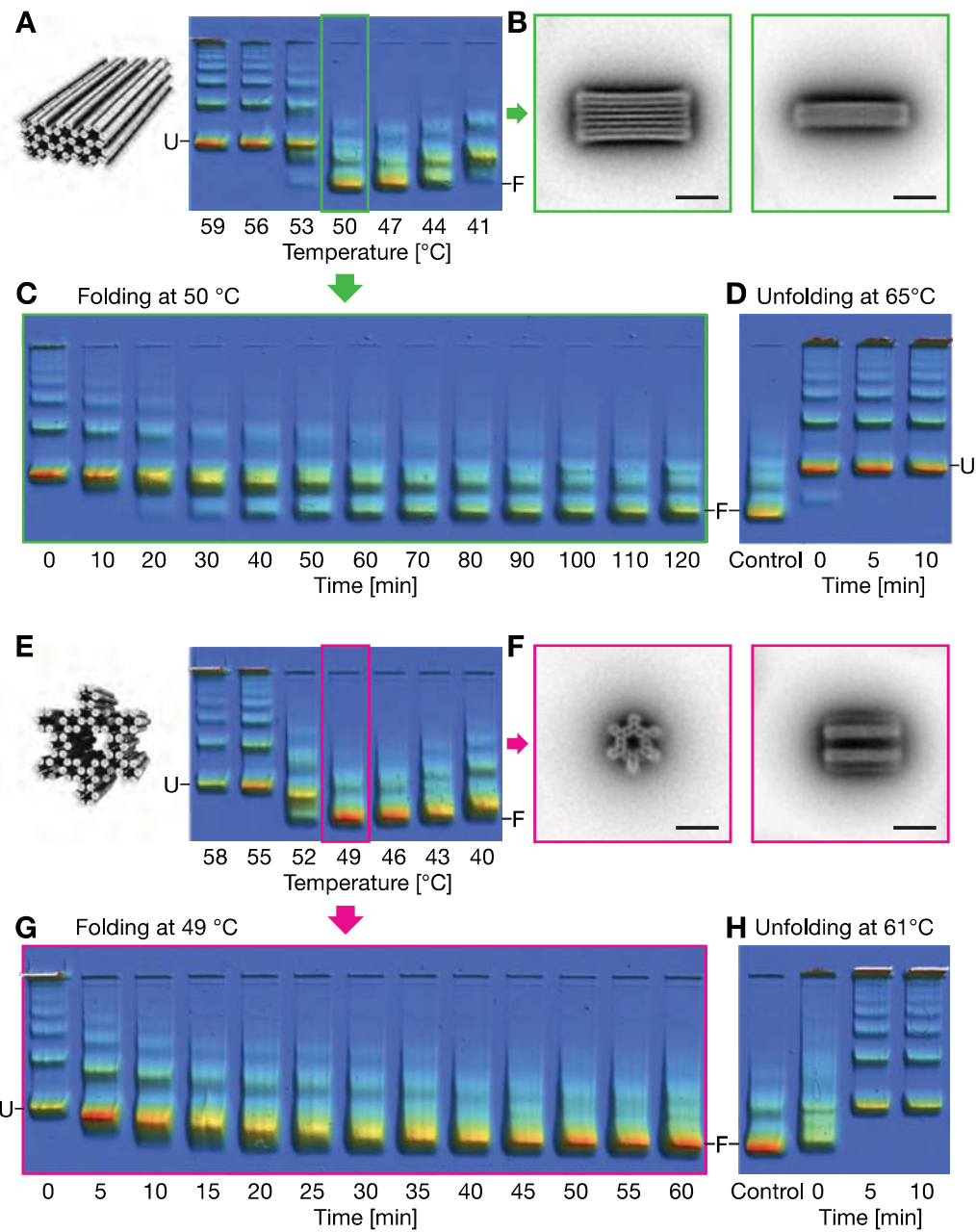


Fig. S8

Time-resolved folding and unfolding of templated 3D DNA objects at constant temperature. **(A)** Agarose gel mobility analysis of the products in reaction mixtures for the brick-like DNA object, exposed to two-hour constant temperature incubation after previous denaturation at 65°C for 15 min. ‘F’ and ‘U’ mark the folded and unfolded species, respectively. **(B)** Average single-particle TEM micrograph obtained from excess-staple free but not otherwise purified products from the reaction mixture exposed to 49°C for 2 hours. Scale bar = 20 nm. See Fig. S9-S19 for additional TEM data. **(C)** Time-resolved folding trajectory of the brick-like DNA object at constant temperature (49°C) as obtained by cryogenic reaction quenching followed by agarose gel electrophoresis. **(D)**

As in (C), but for time-resolved unfolding at the temperature indicated. **(E-H)** As in (A-D), but for the gear-like templated 3D DNA object.

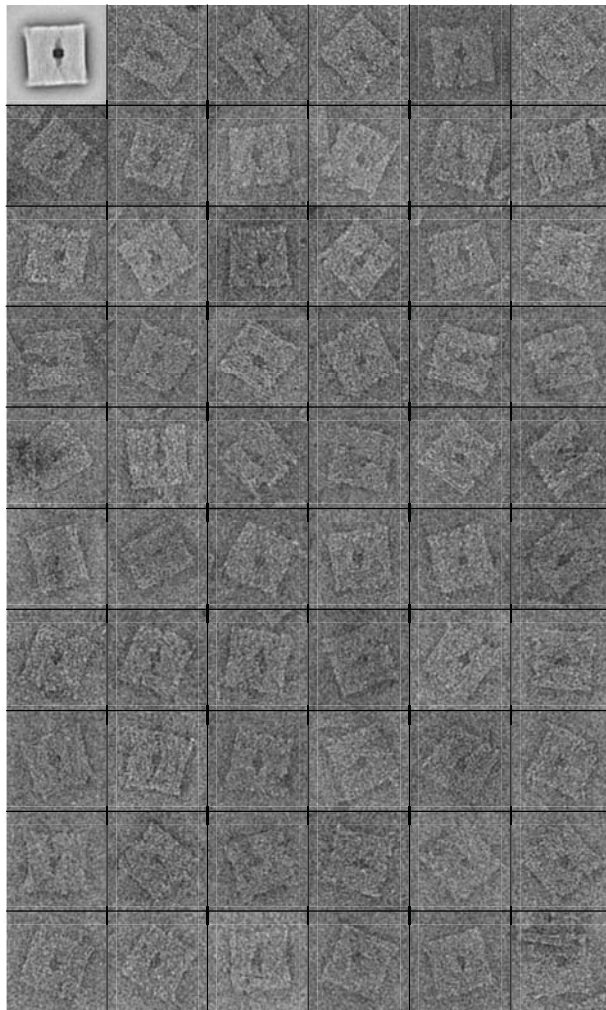


Fig. S9

Typical single particle negative-stain TEM micrographs obtained from filter-purified plate-like DNA objects. Objects were assembled using 2h incubation at 55°C. Excess staple strands were removed by filtration. Box size = 90 nm x 90 nm. Top left object shows the average of all shown structures, after rotational and translational alignment.

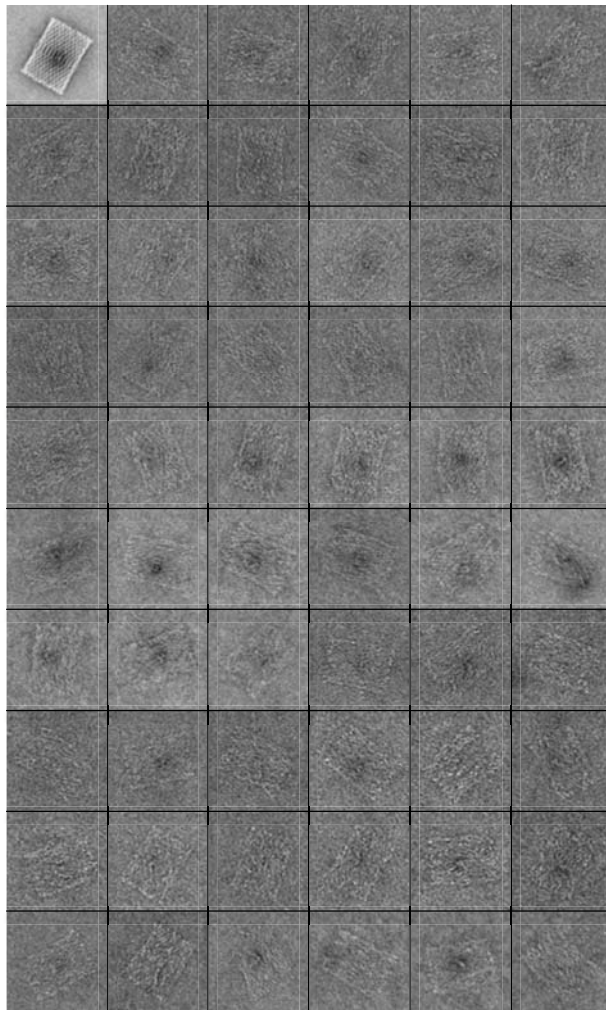


Fig. S10

Typical single particle negative-stain TEM micrographs obtained from filter-purified single-layer rectangle-like DNA objects in the presence of EtBr. Objects were assembled using 5 min incubation at 53°C. Excess staple strands were removed by filtration. Box size = 150 nm x 150 nm. Top left object shows average image of all shown images after rotational and translational alignment. The dark spot in the center of the rectangle is caused by an excess scaffold loop.

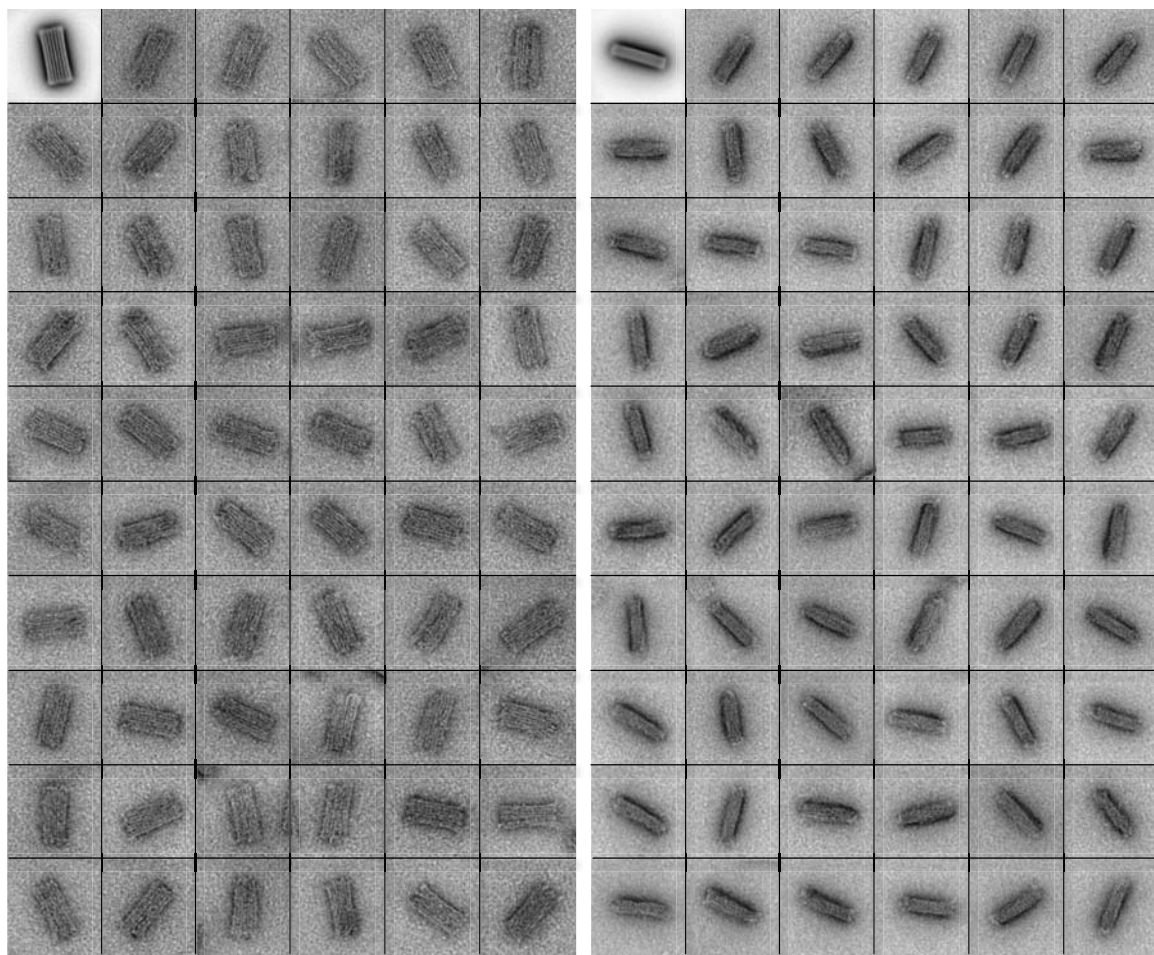


Fig. S11

Negative-stain single-particle TEM micrographs obtained from filter-purified brick-like DNA objects sorted by ‘flat’ (left) and ‘side’ (right) view projections. Objects were assembled using 2h incubation at 50°C. Excess staple strands were removed by filtration. Box size = 90 nm x 90 nm. Top left object shows average image after rotational and translational alignment of all the images shown, respectively.

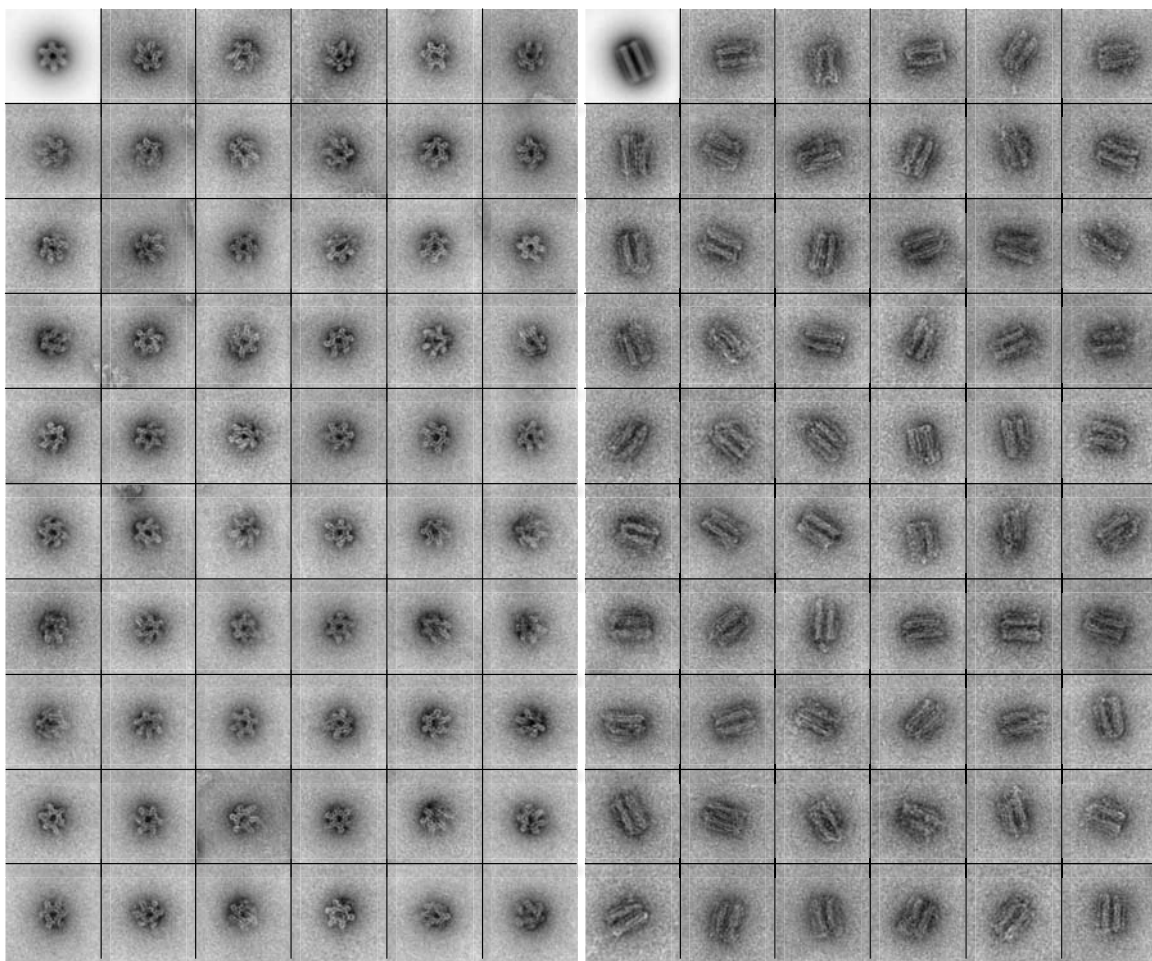


Fig. S12

Typical single-particle negative-stain TEM micrographs obtained from filter-purified gear-like DNA objects sorted by ‘front’ (left) and ‘side’ (right) view projections. Objects were assembled using 2h incubation at 49°C. Excess staple strands were removed by filtration. Box size = 90 nm x 90 nm. Top left: average image of all images shown after rotational and translational alignment.

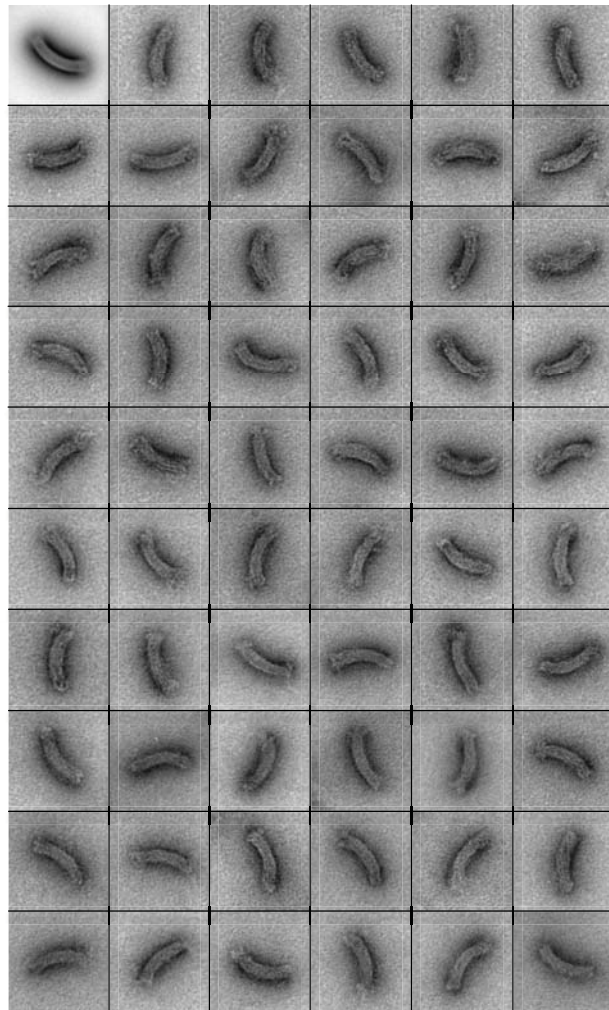
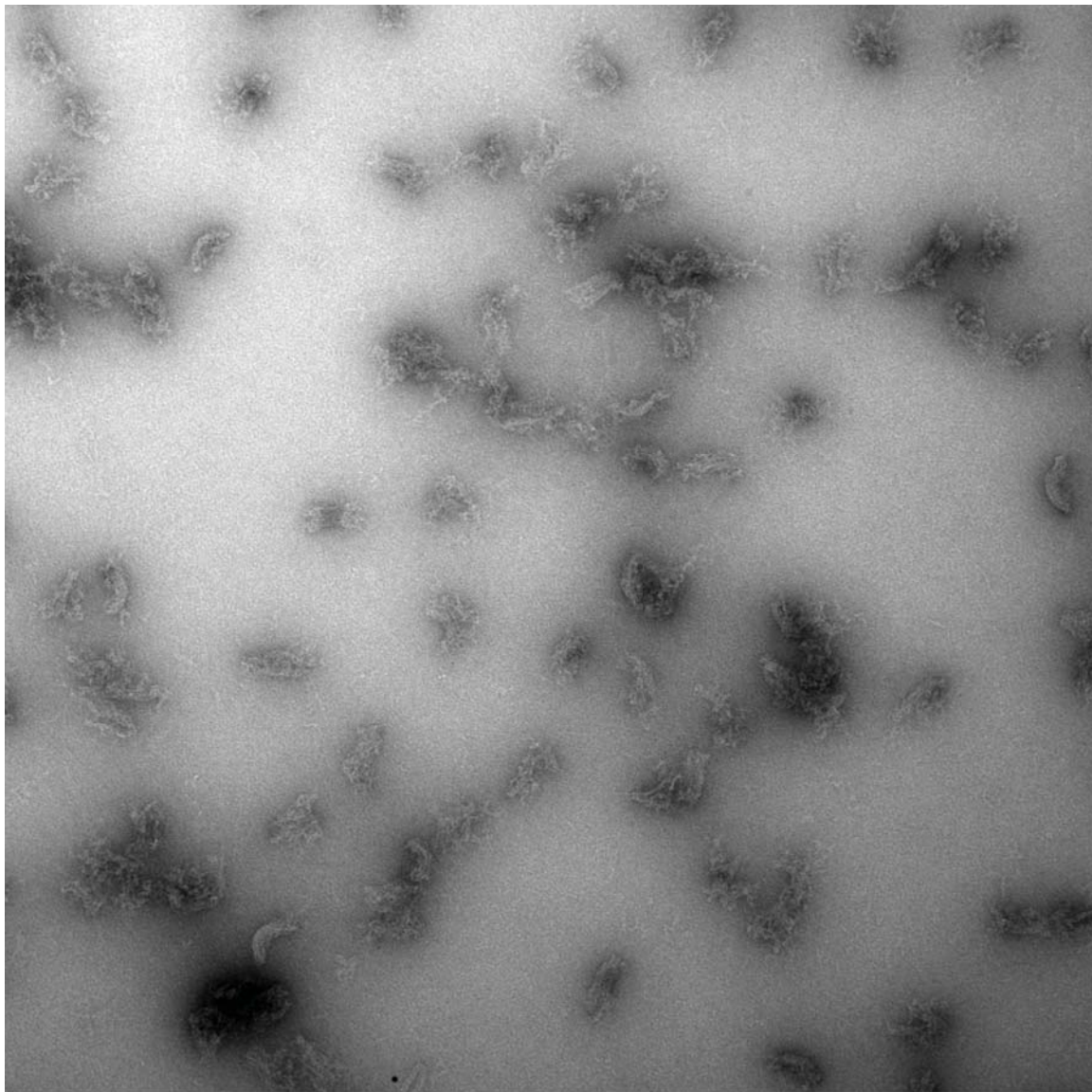


Fig. S13

Typical single-particle negative-stain TEM micrographs obtained from filter-purified brick-like DNA objects with moderate degree of bending. Objects were assembled using stepwise cooling from 65°C to 25°C with a rate of 1°C/h. Excess staple strands were removed by filtration. Box size = 90 nm x 90 nm. Top left object shows average image obtained after rotational and translational alignment of all images shown.



2012.06.06 42hbv10 filt puri 5sec G 3-A-7052
2012.06.06 42hbv10 filt puri 5sec G 3-A-7
Cal: 0.455581 nm/pix

100 nm
HV=100.0kV
Direct Mag: 28500x
BioNano TEM Facility

Fig. S14

Typical field-of-view negative-stain TEM micrograph obtained from filter-purified brick-like DNA objects with strong degree of bending (see Fig. 2). Reactions were subjected to stepwise cooling from 65°C to 25°C with a rate of 1°C/h, but the objects failed to fold. Note that a distinct peak in the rate-of-folding data was lacking in the fluorometric analysis performed for this assembly reaction mixture (Fig. 2). Staple strands were removed by filtration.

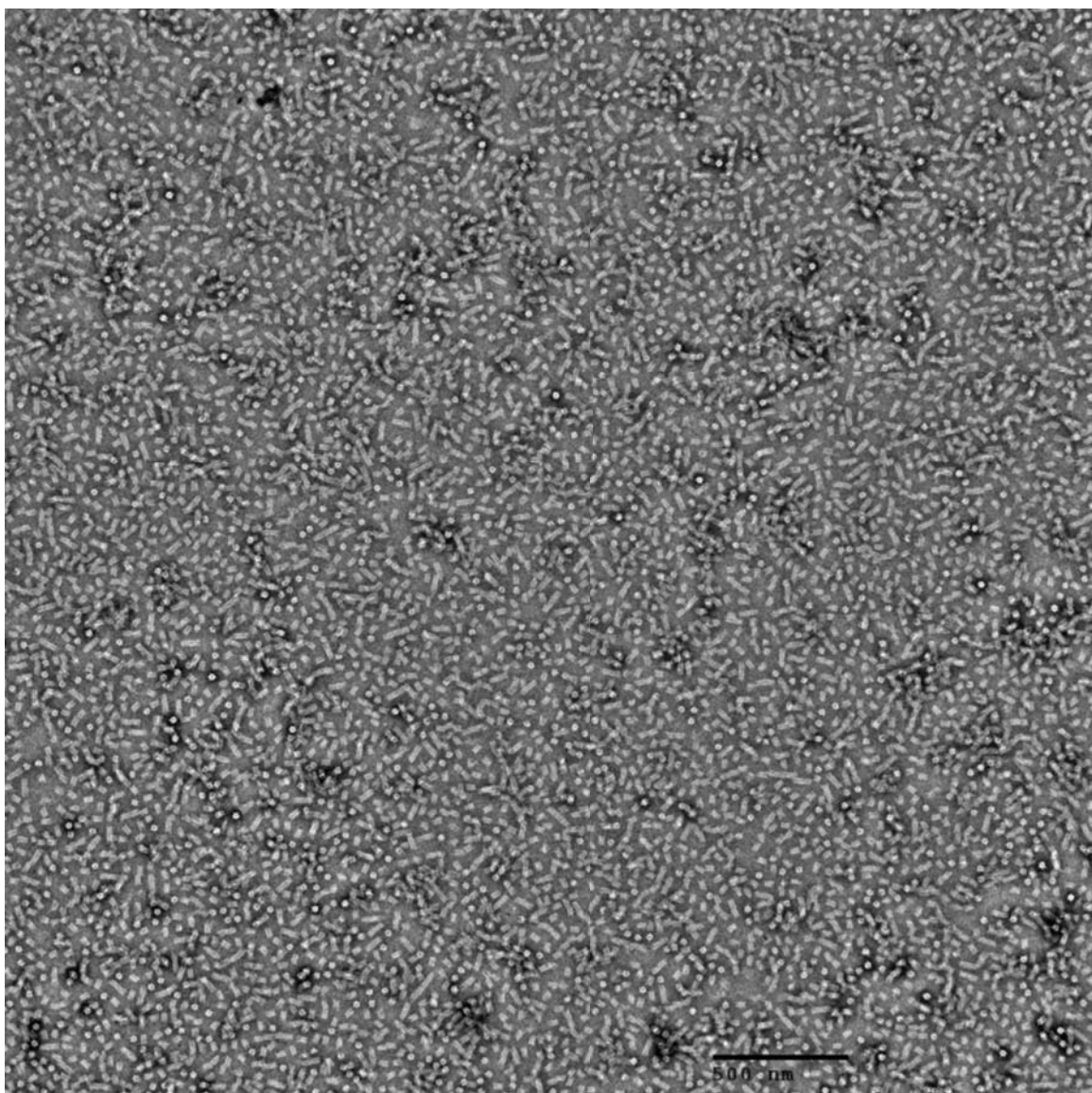


Fig. S15

Typical field-of-view negative-stain TEM micrograph obtained from filter-purified gear-like DNA objects. Objects were assembled using 2h incubation at 49°C. Excess staple strands were removed by filtration.

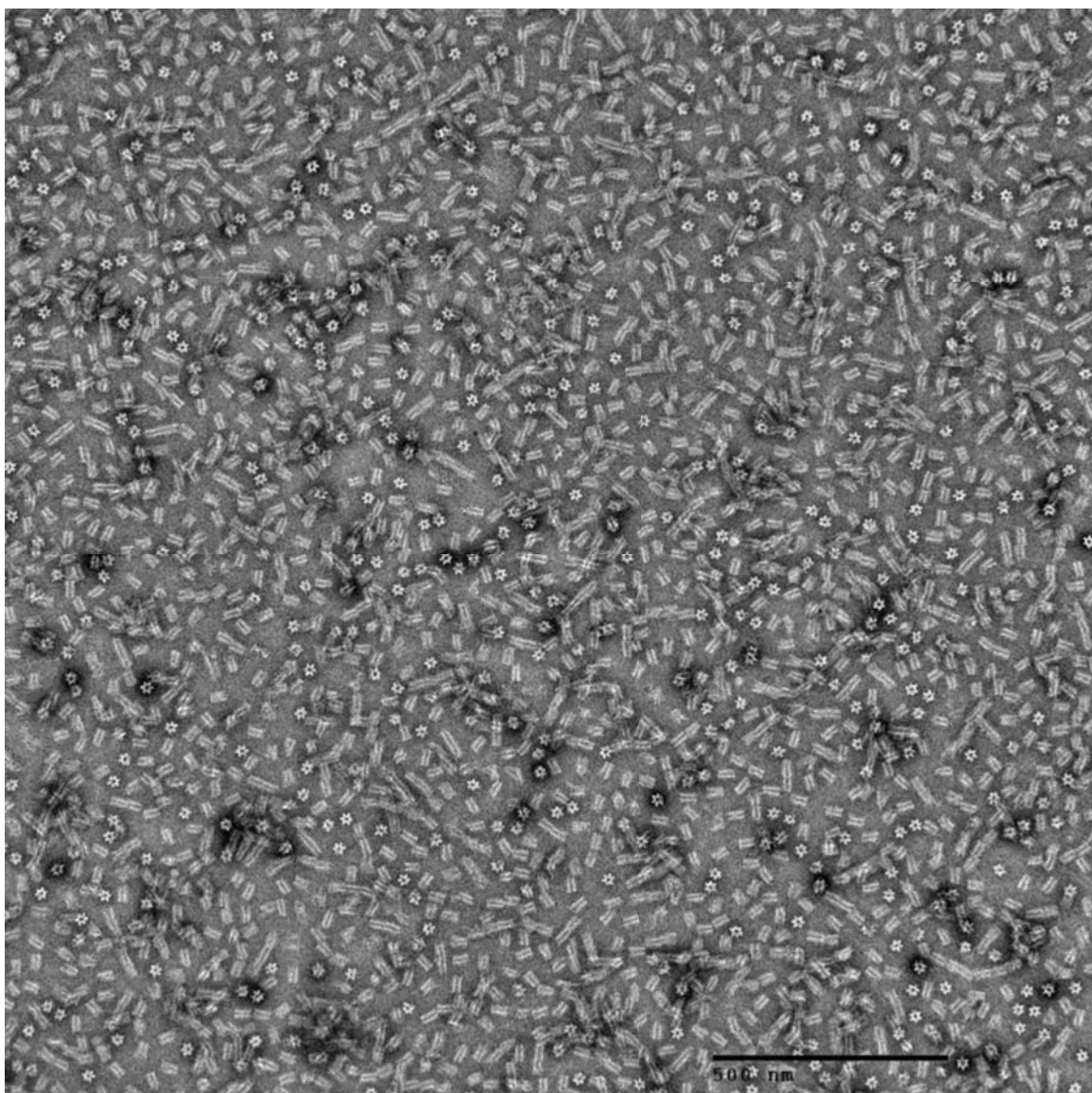


Fig. S16

Typical field-of-view negative-stain TEM micrograph obtained from filter-purified gear-like DNA objects. Objects were assembled using 2h incubation at 49°C. Excess staple strands were removed by filtration.

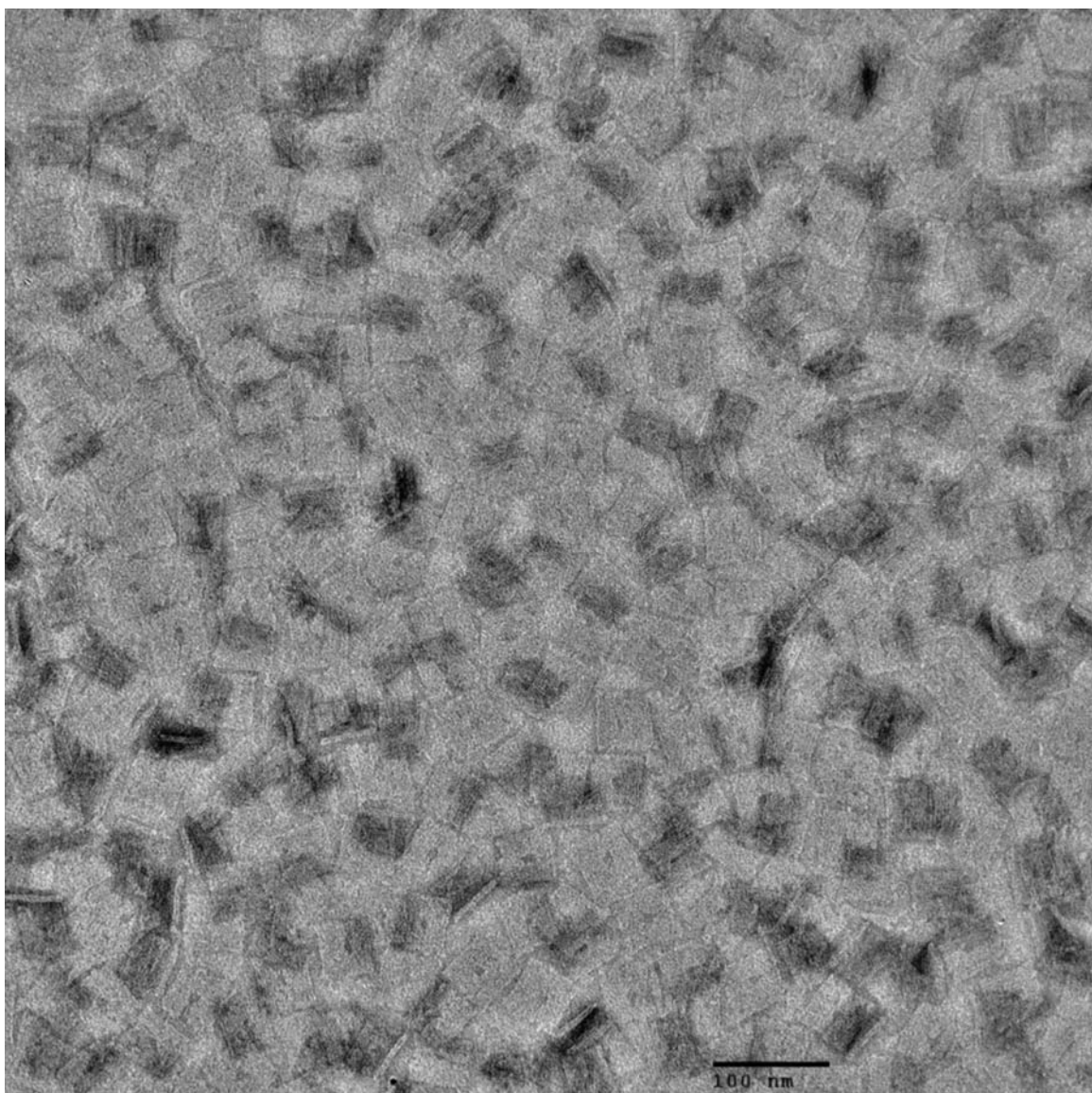


Fig. S17

Typical field-of-view negative-stain TEM micrograph obtained from filter-purified plate-like DNA objects. Objects were assembled using 2h incubation at 55°C. Excess staple strands were removed by filtration.

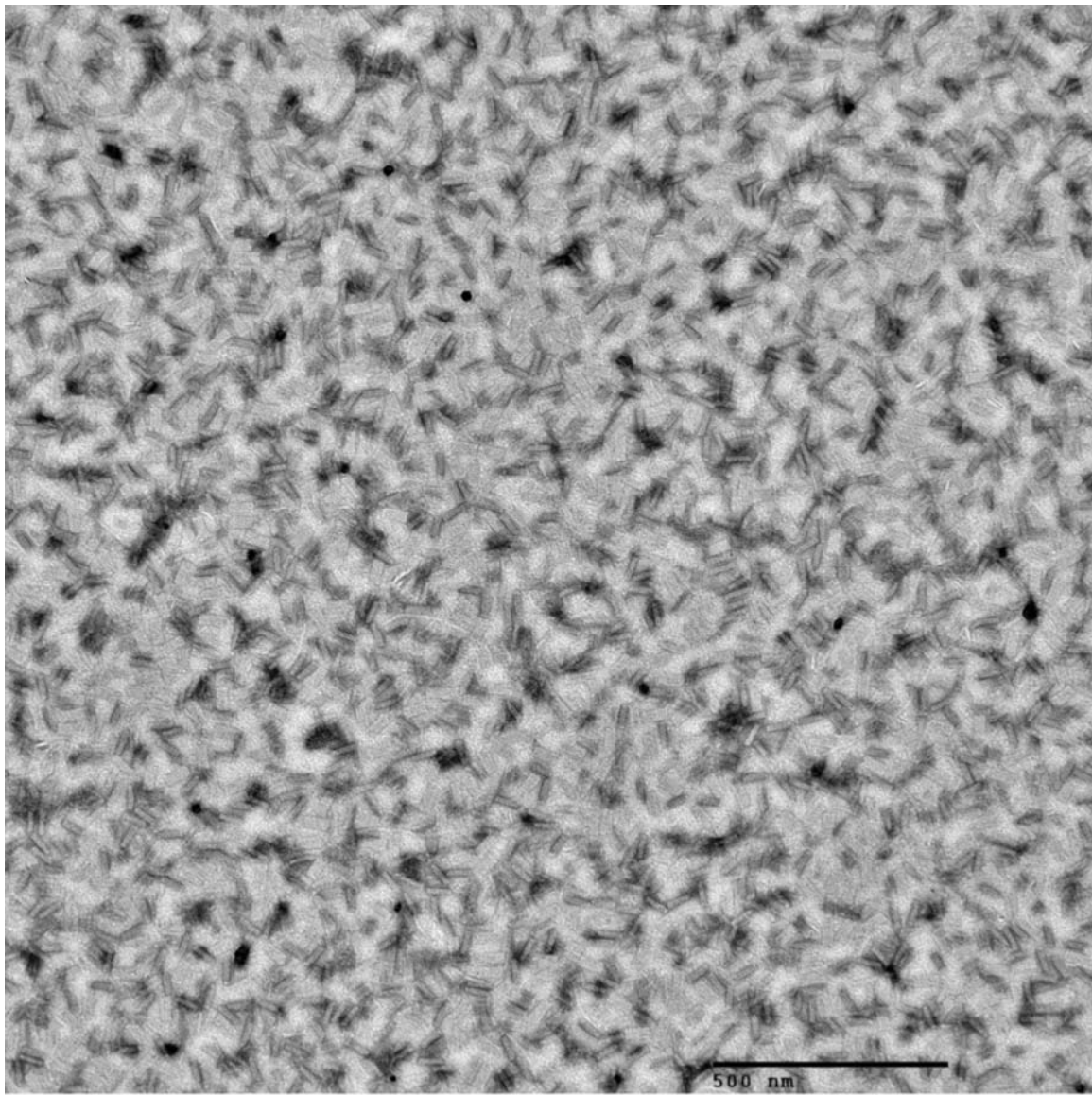


Fig. S18

Typical field-of-view negative-stain TEM micrograph obtained from filter-purified brick-like DNA objects. Objects were assembled using 2h incubation at 50°C. Excess staple strands were removed by filtration.

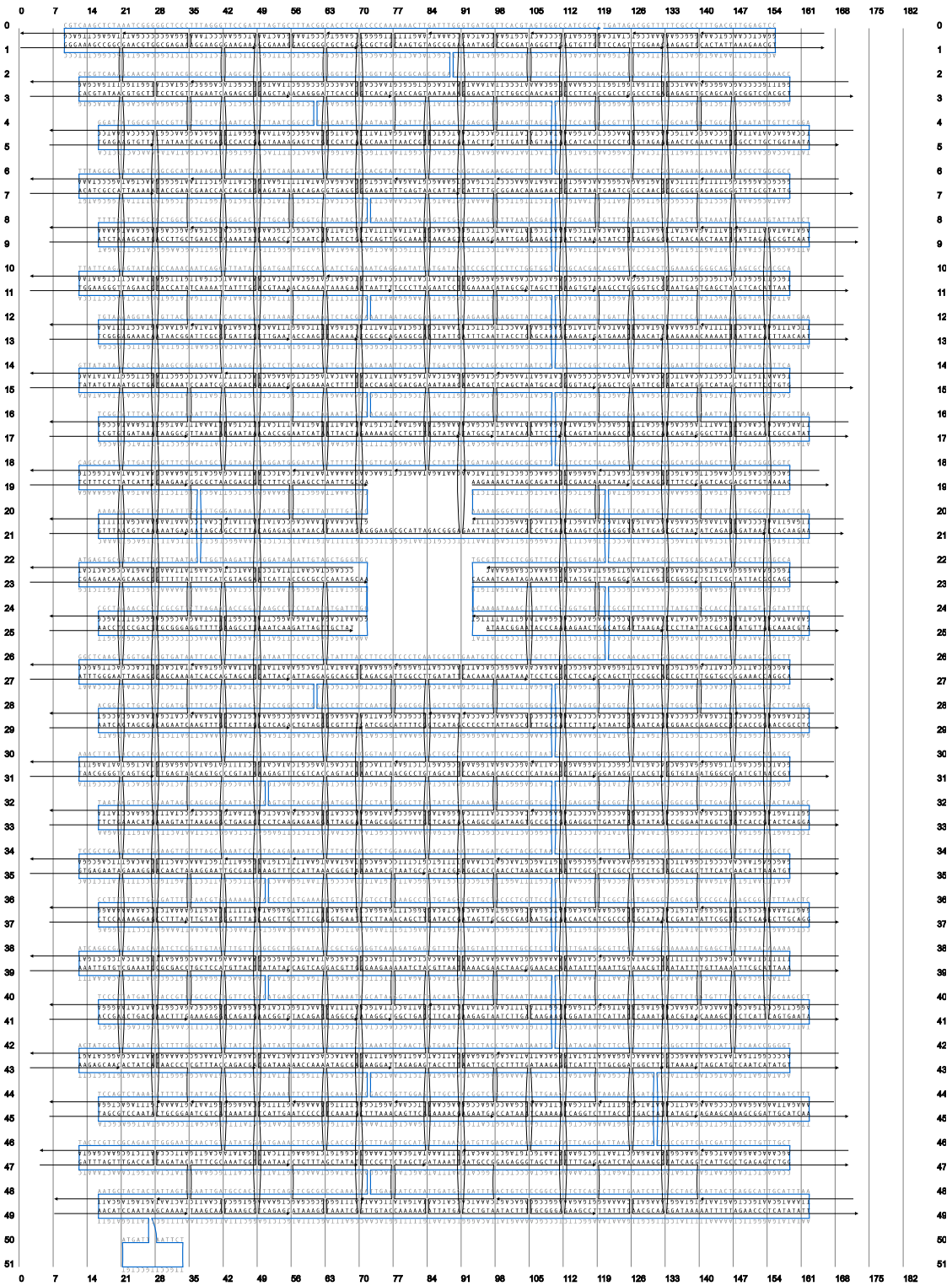


Fig. S19

Strand routing diagram: plate-like object

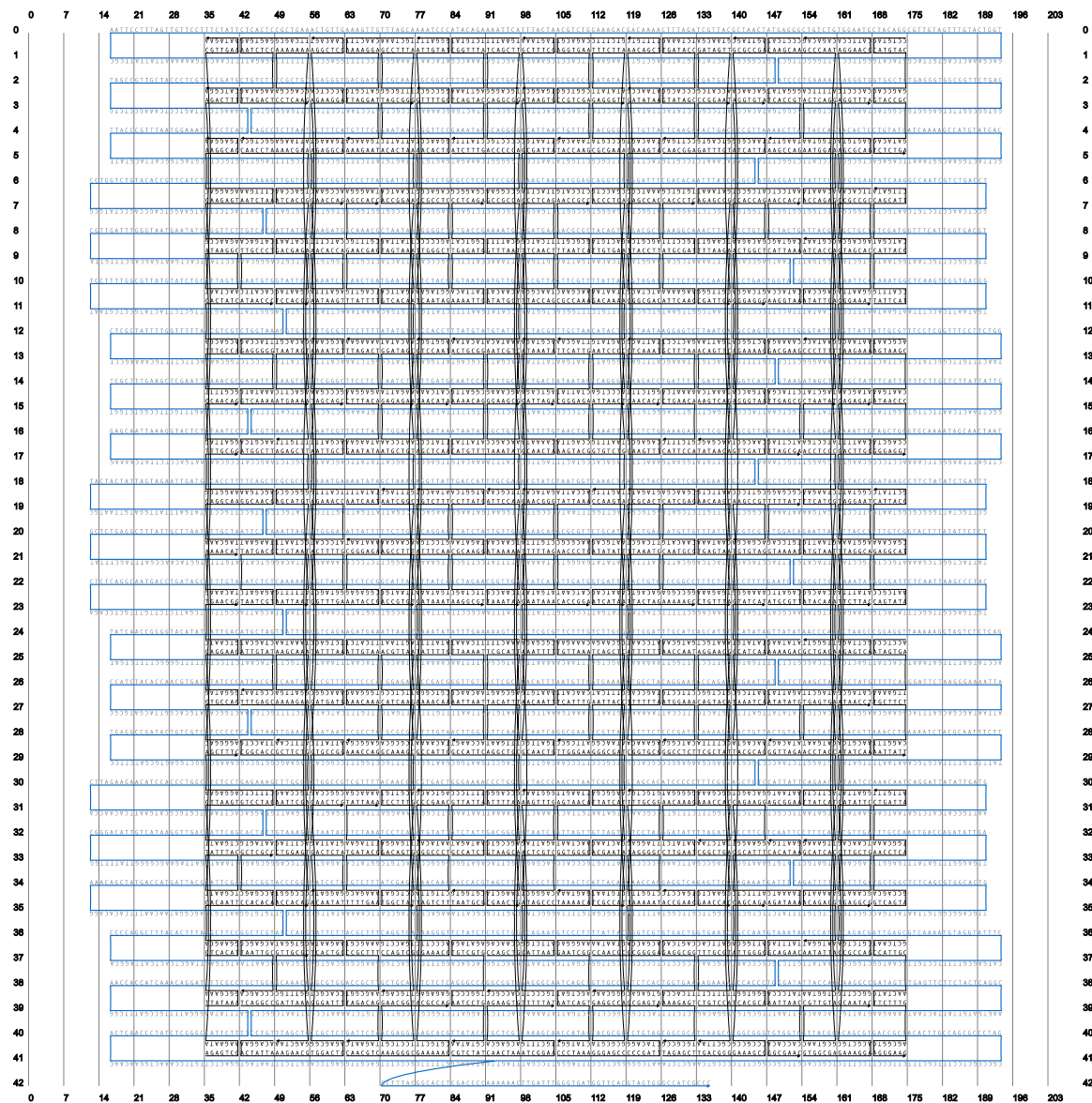


Fig. S20

Strand routing diagram: brick-like object

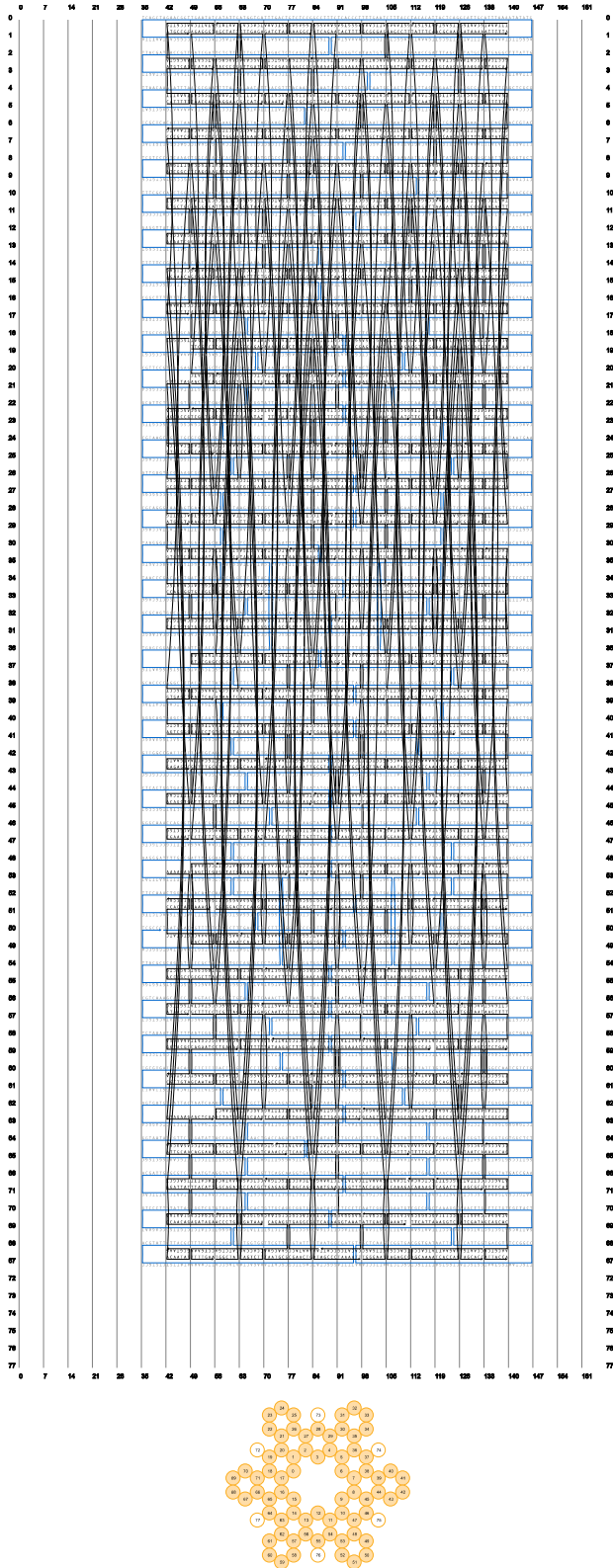
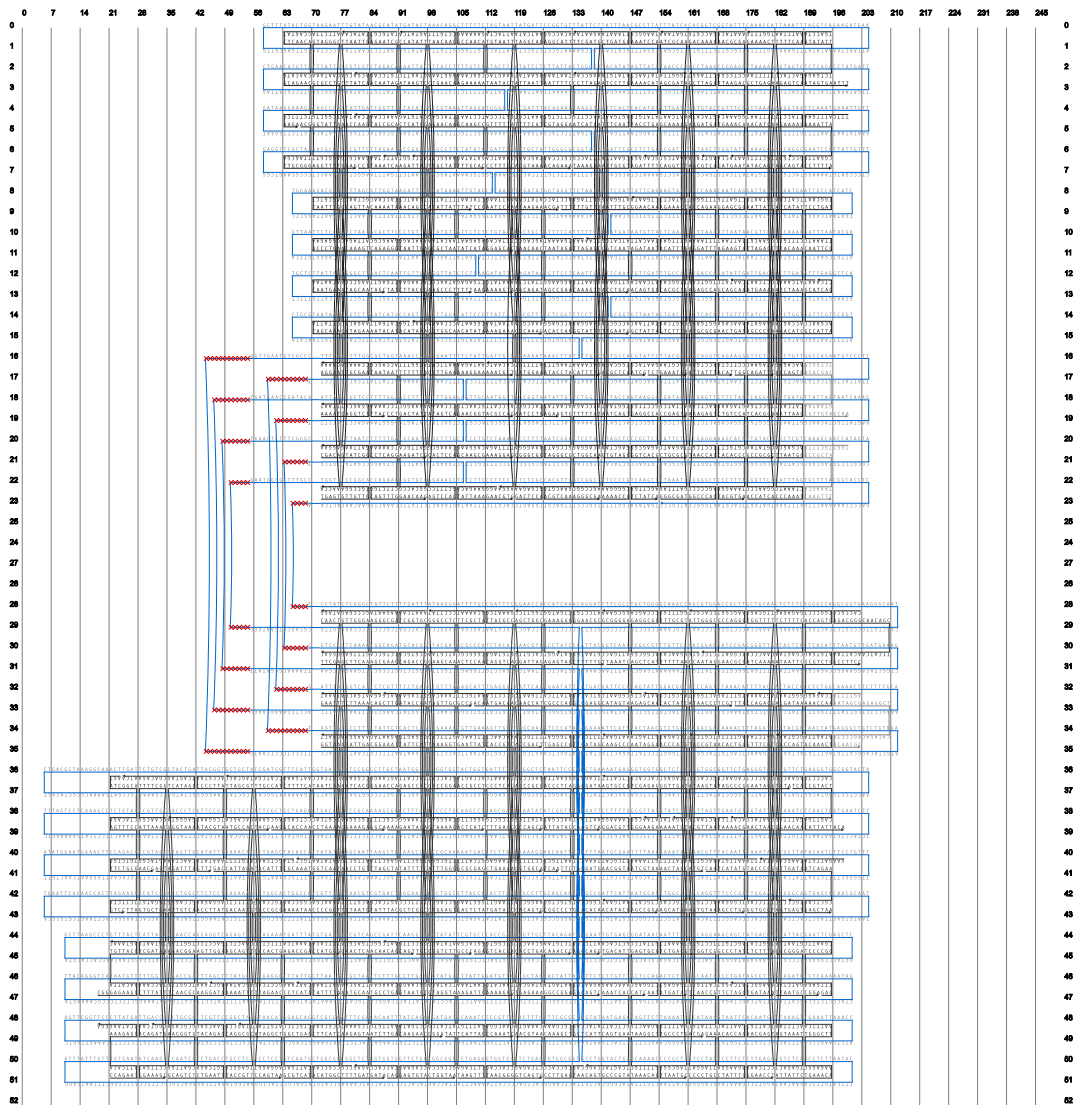


Fig. S21
Strand routing diagram: gear-like object



37
38
39
40
41
42
43
44
45
46
47
48
49
50
51
52
53
54
55
56
57
58
59
60

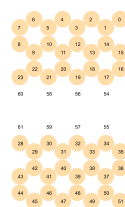


Fig. S22

Strand routing diagram: hinged-bar object

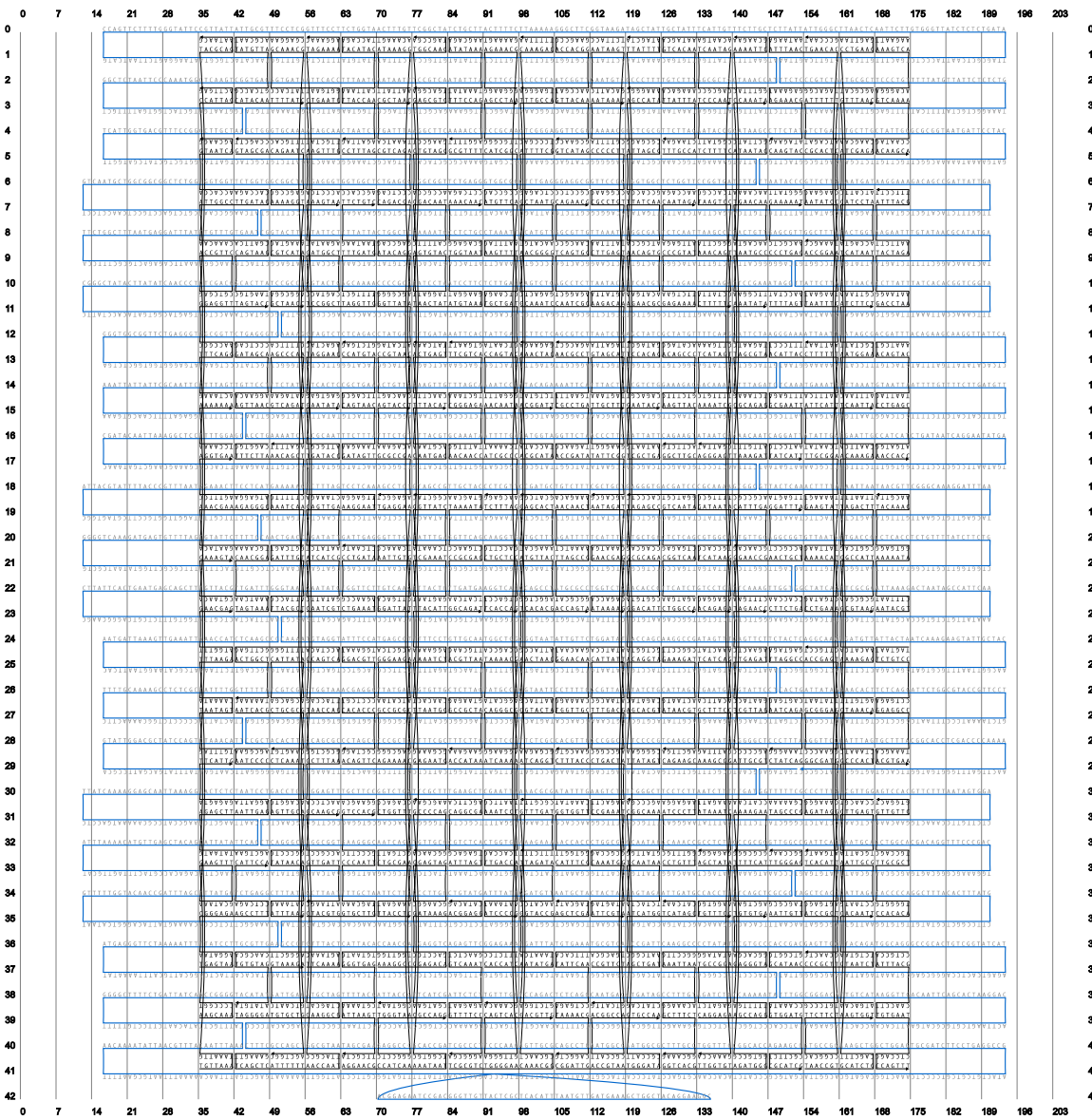


Fig. S23

Strand routing diagram: brick-like object, sequence permutation #1

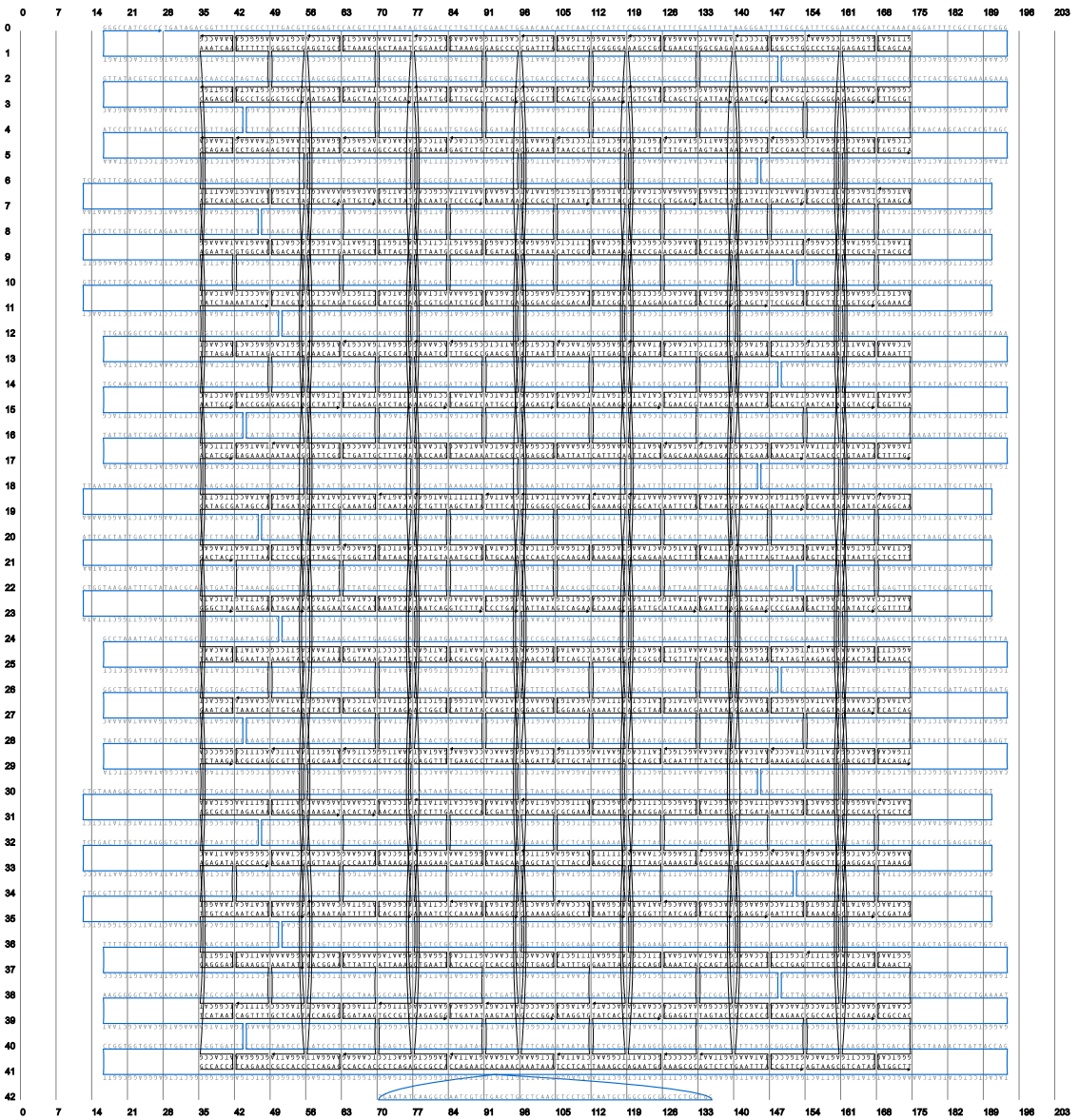


Fig. S24

Strand routing diagram: brick-like object, sequence permutation #2

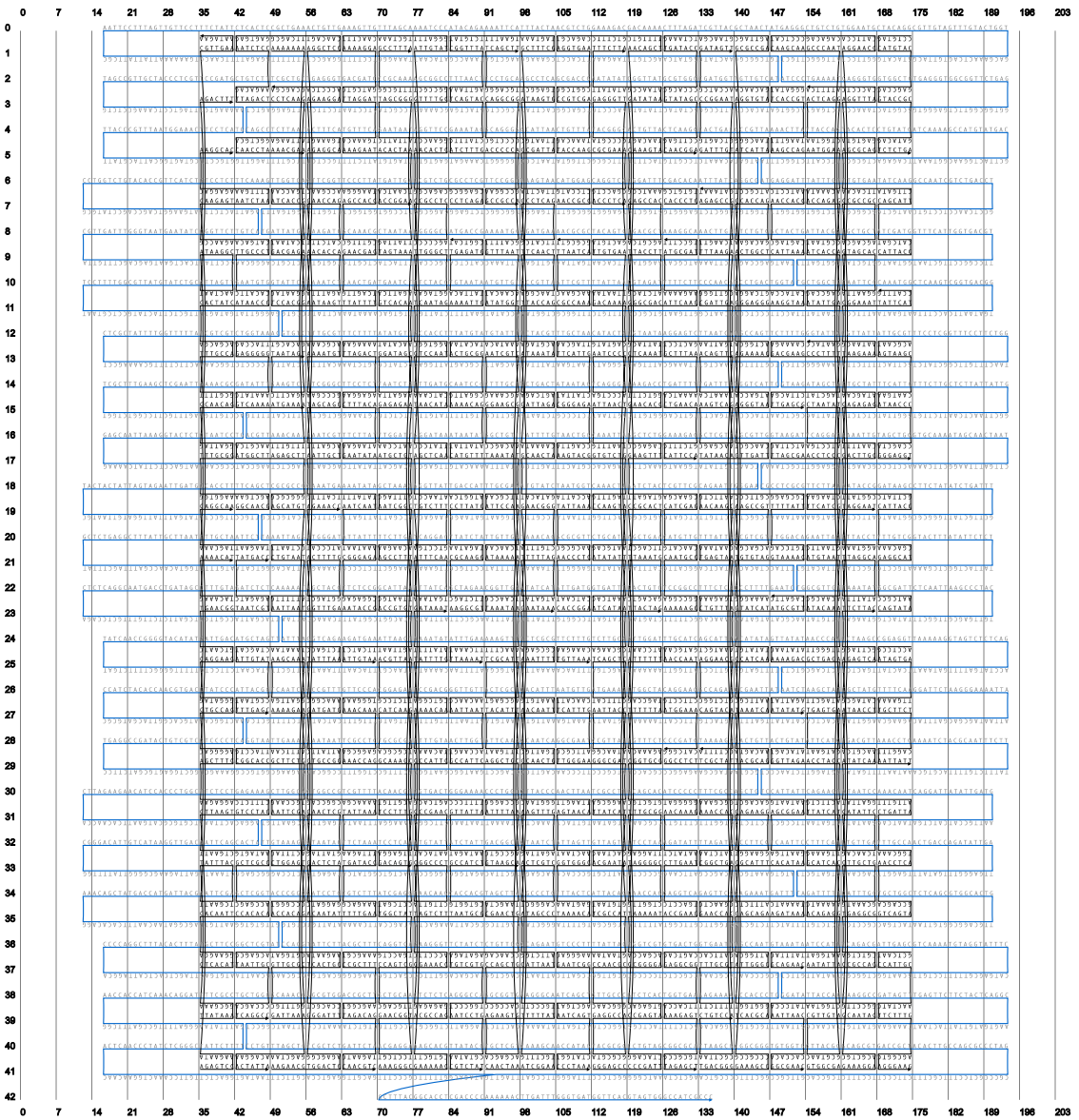


Fig. S25

Strand routing diagram: brick-like object, long staple strands

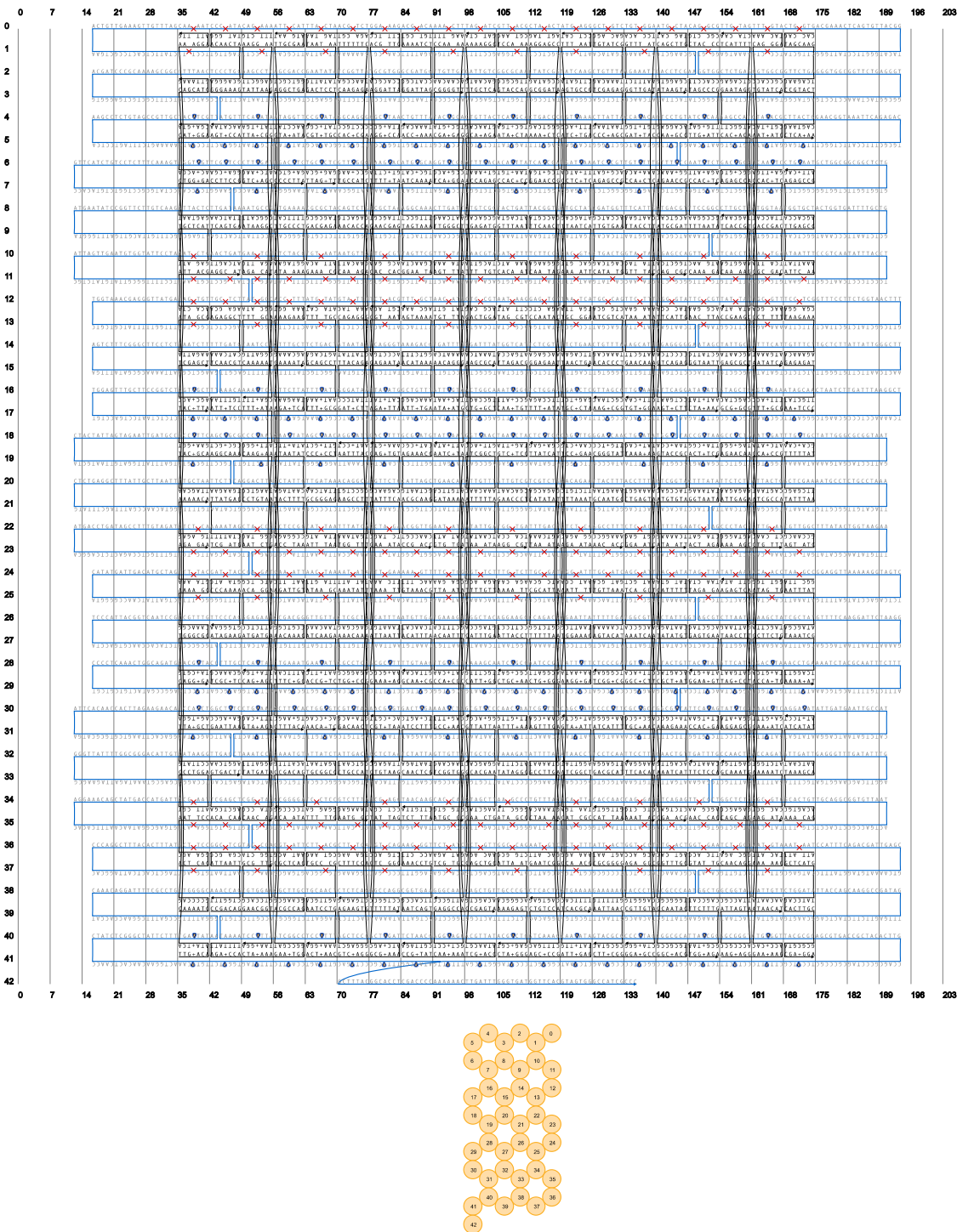


Fig. S26

Strand routing diagram: brick-like object, moderate bend

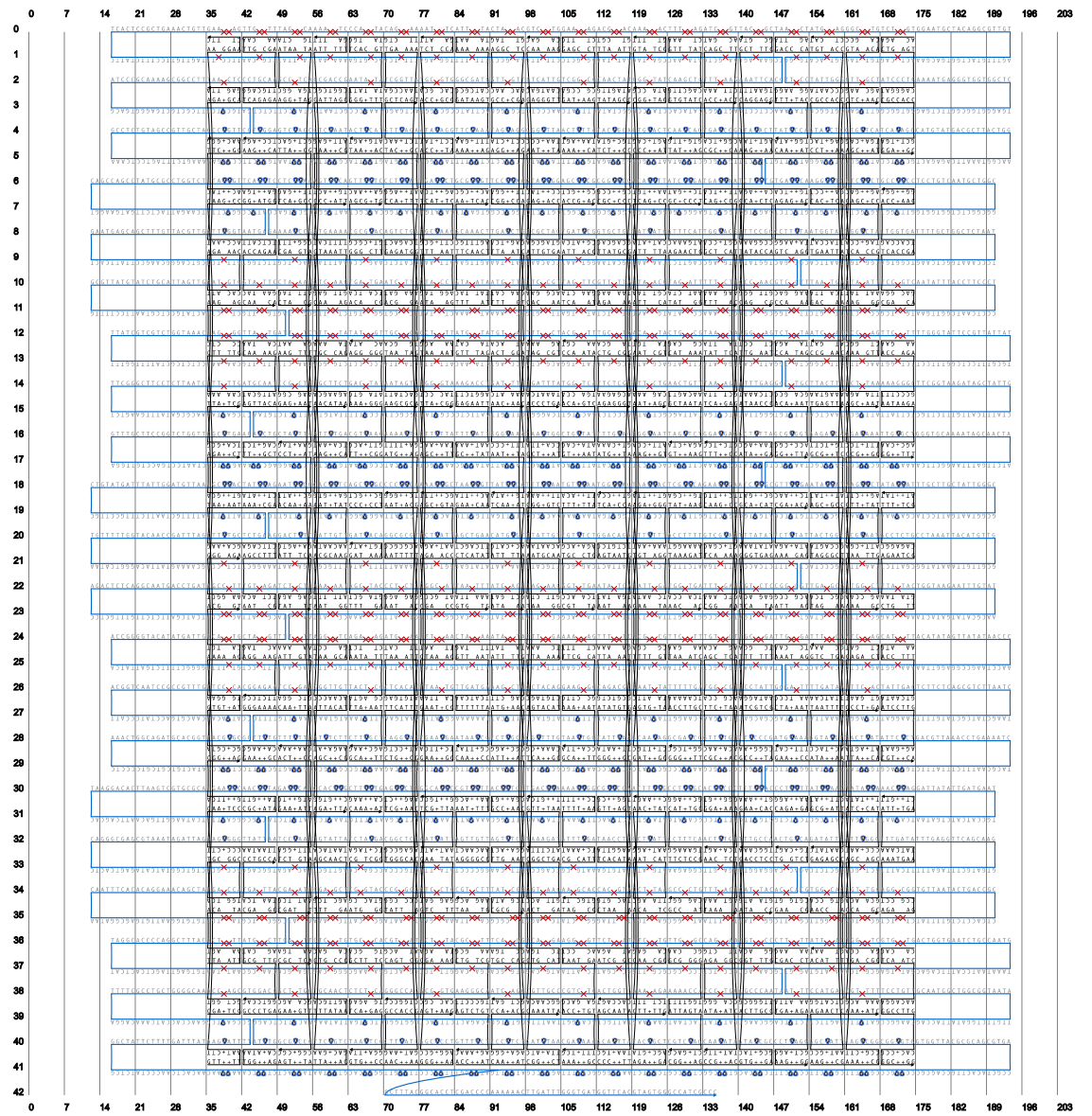


Fig. S27

Strand routing diagram: brick-like object, strong bend

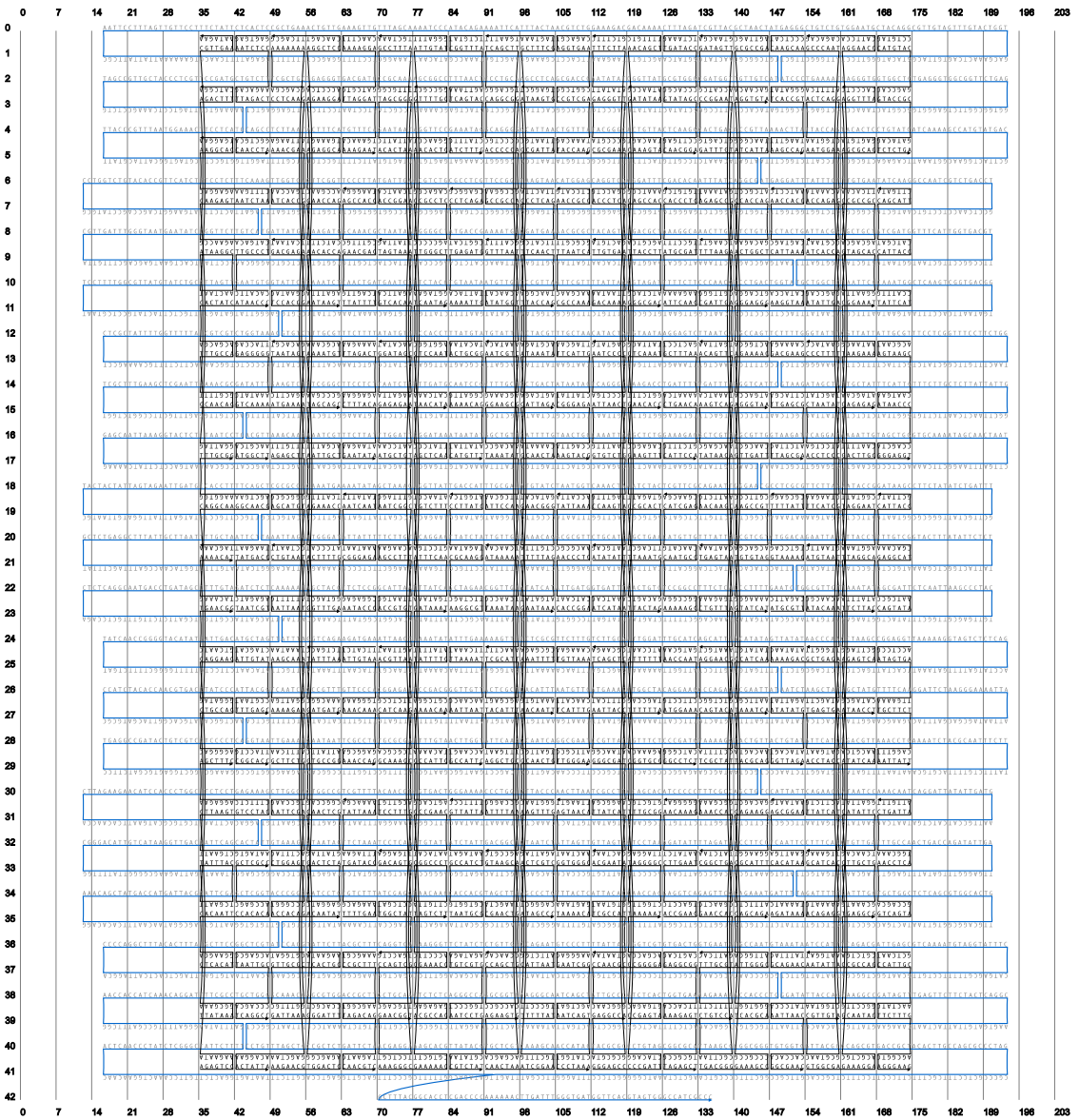


Fig. S28

Strand routing diagram: brick-like object, staple strand breaking variation A

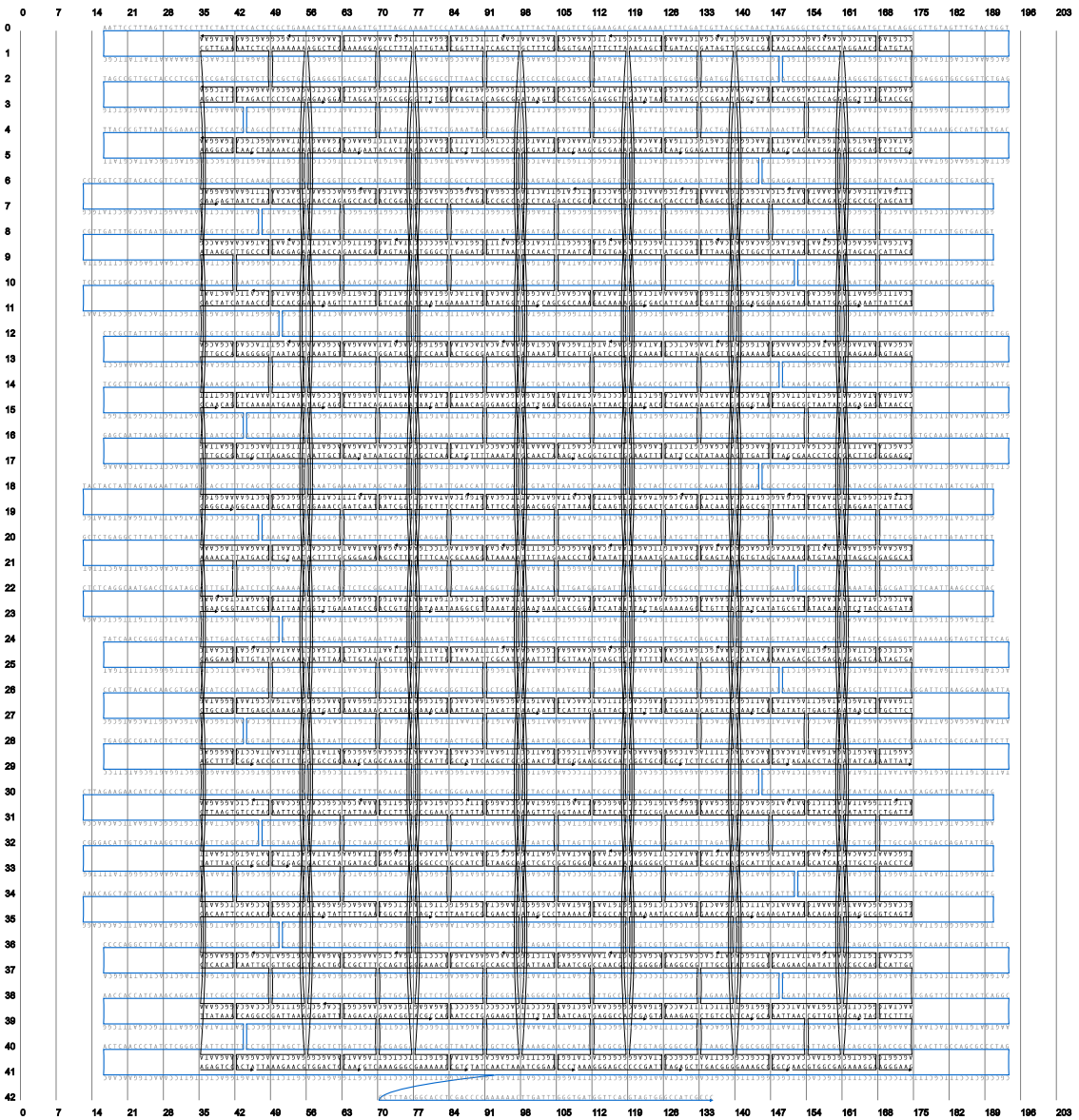


Fig. S29

Strand routing diagram: brick-like object, staple strand breaking variation B

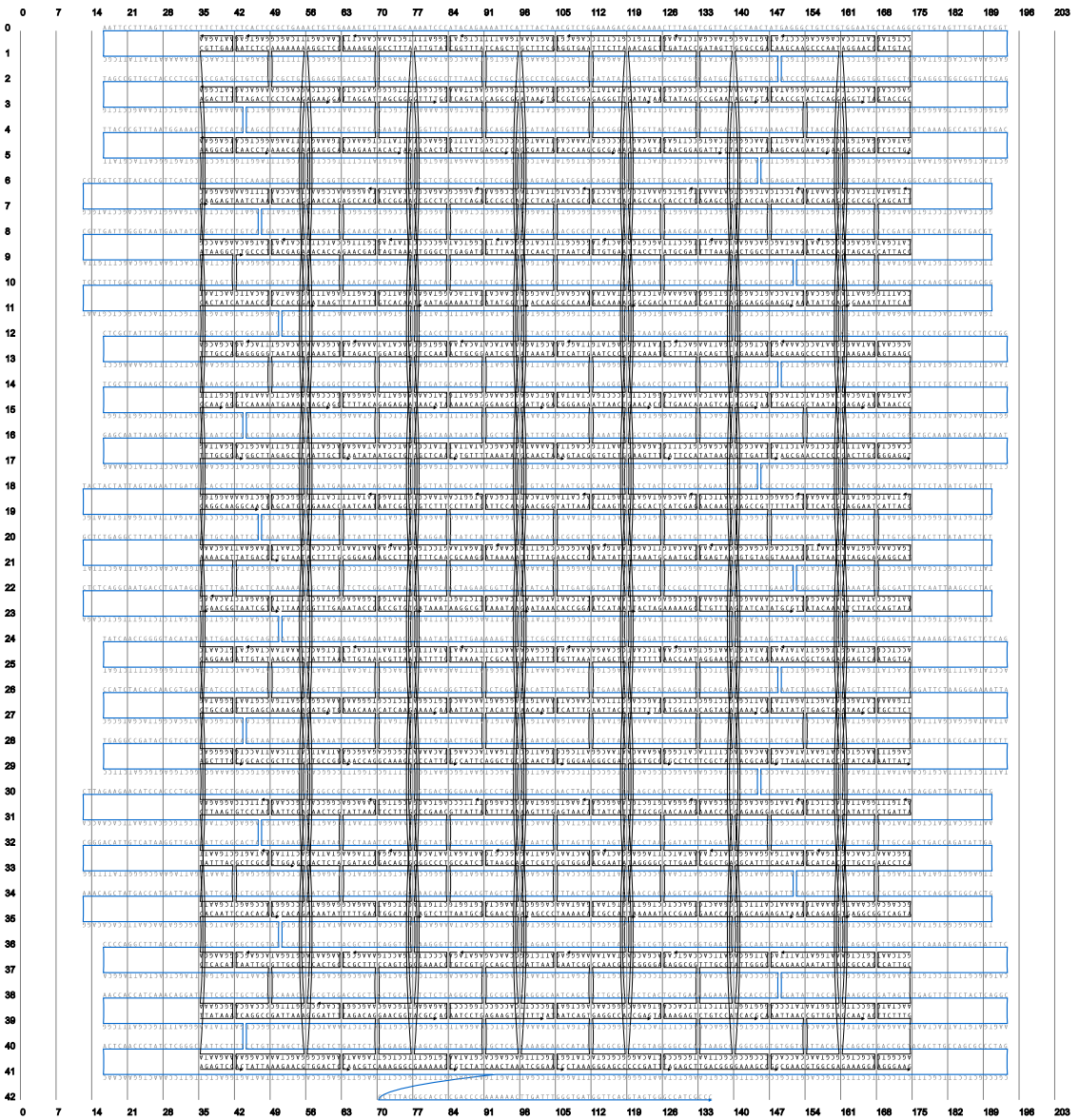


Fig. S30

Strand routing diagram: brick-like object, staple strand breaking variation C

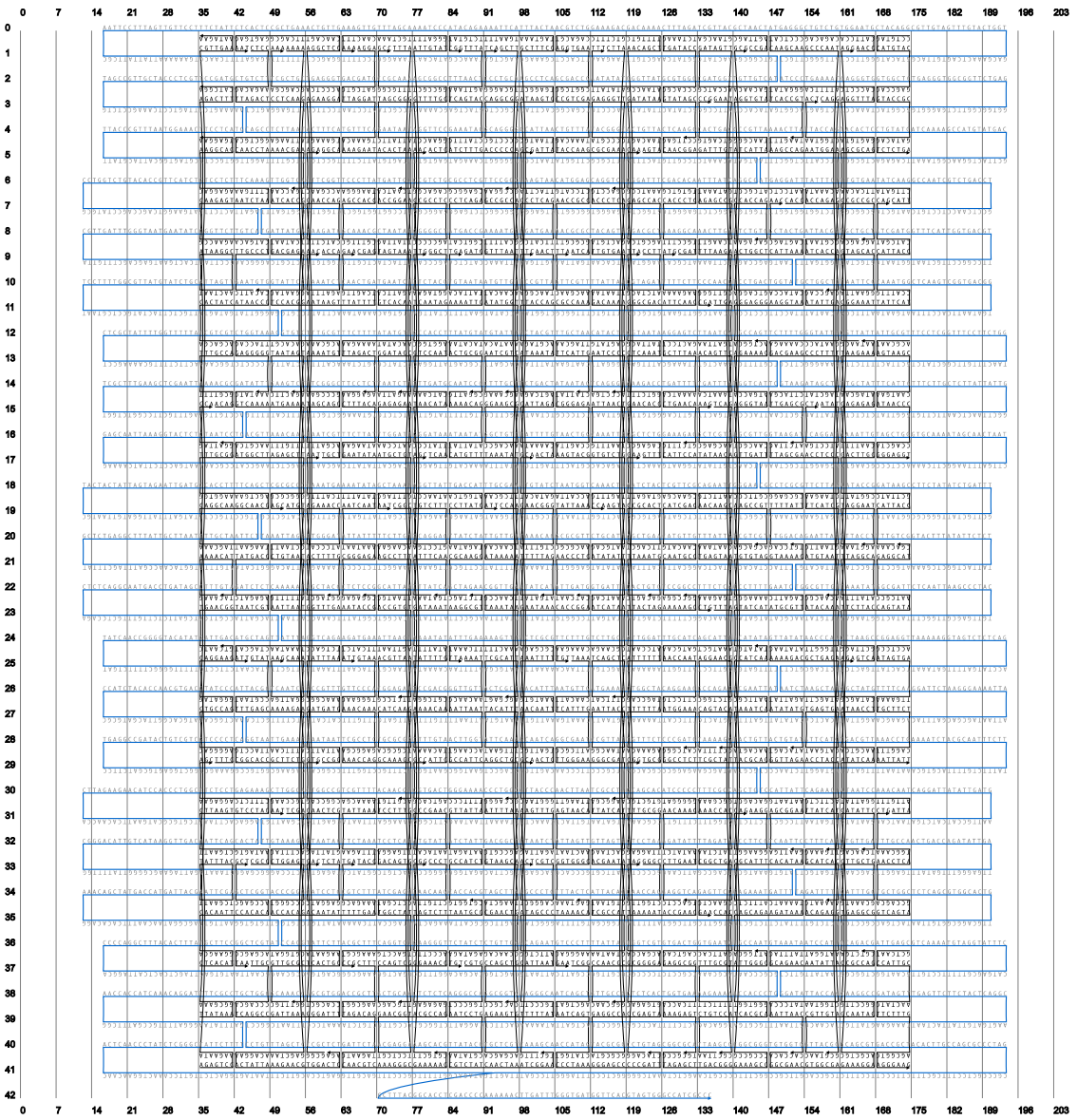


Fig. S31

Strand routing diagram: brick-like object, staple strand breaking variation D

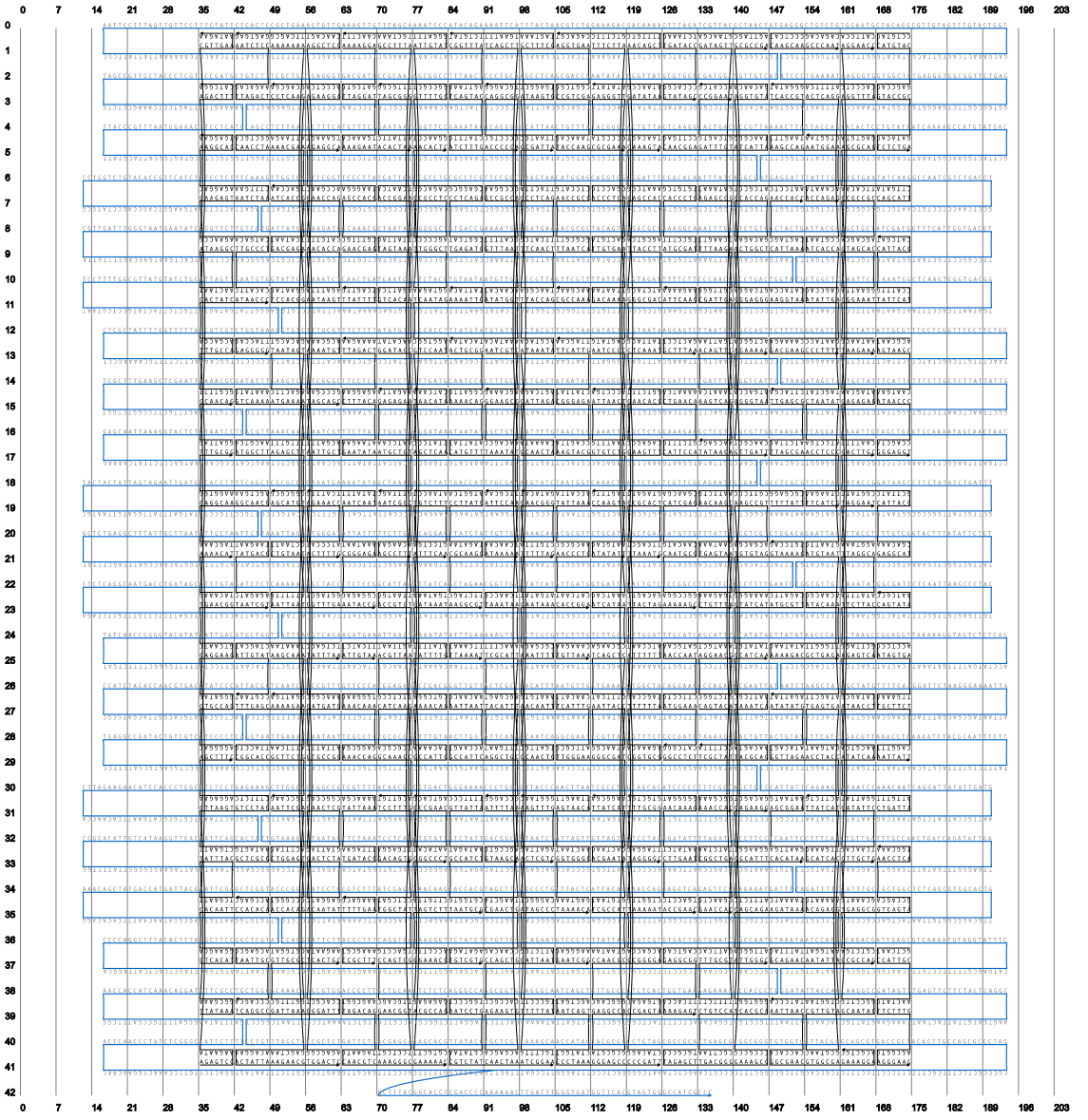


Fig. S32

Strand routing diagram: brick-like object, staple strand breaking variation E

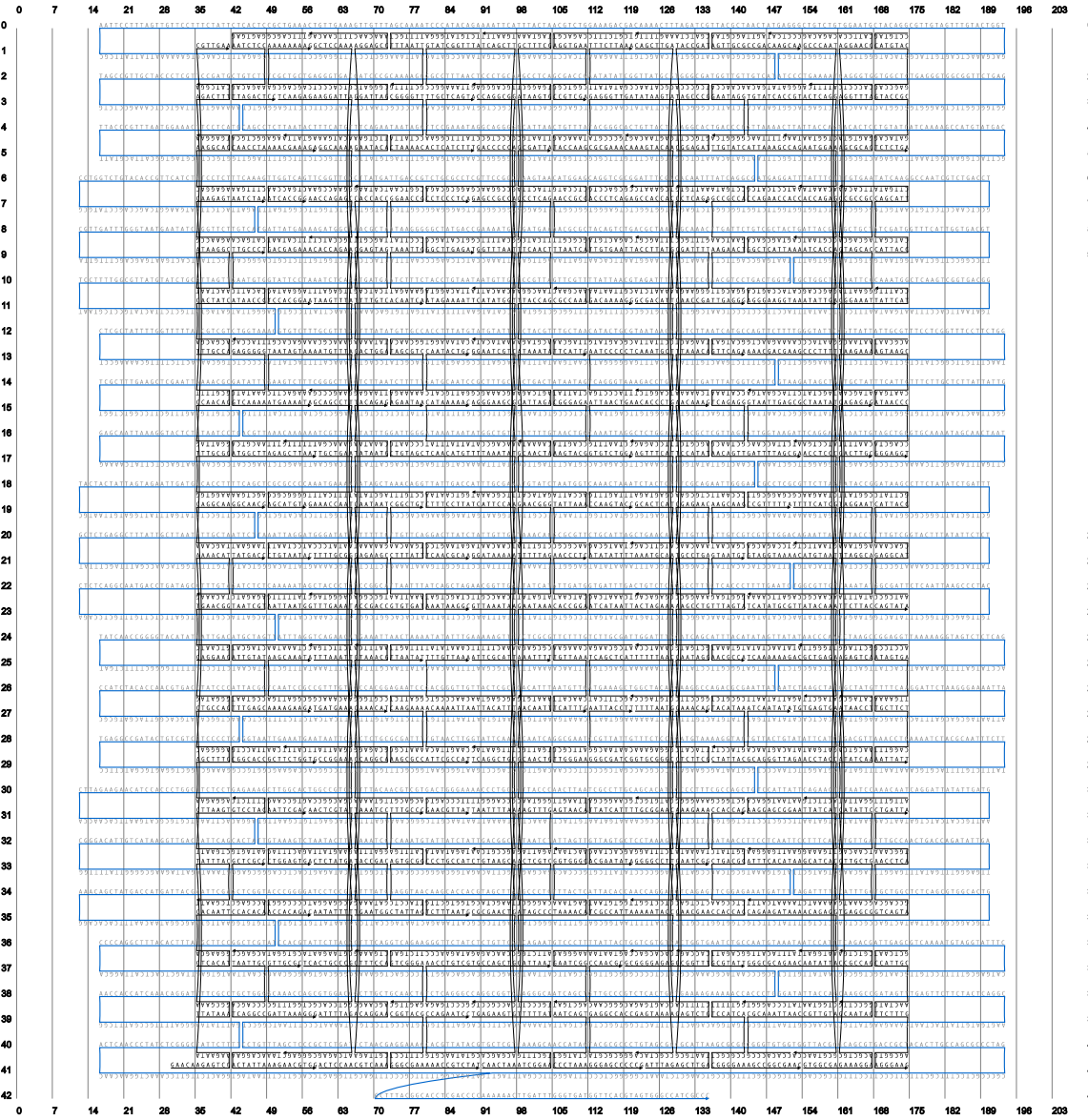


Fig. S33

Strand routing diagram: brick-like object, staple strand breaking variation F

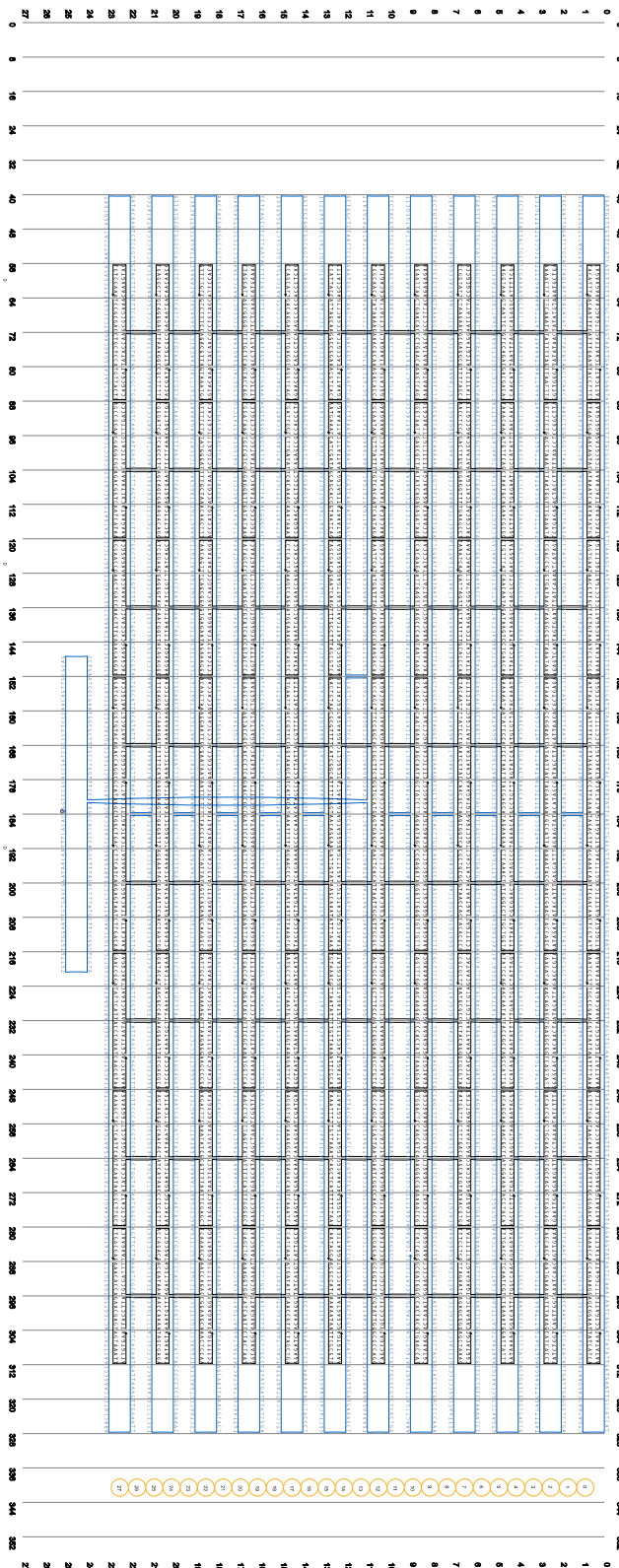


Fig. S34

Strand routing diagram: single layer rectangle

Additional Data table S1 (separate file)

In this file staple oligonucleotide sequences for the plate-like object are provided.

Additional Data table S2 (separate file)

In this file staple oligonucleotide sequences for the brick-like object are provided.

Additional Data table S3 (separate file)

In this file staple oligonucleotide sequences for the gear-like object are provided.

Additional Data table S4 (separate file)

In this file staple oligonucleotide sequences for the hinged-bar object are provided.

Additional Data table S5 (separate file)

In this file staple oligonucleotide sequences for the brick-like object with sequence permutation 1 are provided.

Additional Data table S6 (separate file)

In this file staple oligonucleotide sequences for the brick-like object with sequence permutation 2 are provided.

Additional Data table S7 (separate file)

In this file staple oligonucleotide sequences for the brick-like object with sequence mismatches are provided.

Additional Data table S8 (separate file)

In this file staple oligonucleotide sequences for the brick-like object with long staple strands are provided.

Additional Data table S9 (separate file)

In this file staple oligonucleotide sequences for the brick-like object with moderate bend are provided.

Additional Data table S10 (separate file)

In this file staple oligonucleotide sequences for the brick-like object with strong bend are provided.

Additional Data table S11 (separate file)

In this file staple oligonucleotide sequences for the brick-like object with staple strand breaking variation A are provided.

Additional Data table S12 (separate file)

In this file staple oligonucleotide sequences for the brick-like object with staple strand breaking variation B are provided.

Additional Data table S13 (separate file)

In this file staple oligonucleotide sequences for the brick-like object with staple strand breaking variation C are provided.

Additional Data table S14 (separate file)

In this file staple oligonucleotide sequences for the brick-like object with staple strand breaking variation D are provided.

Additional Data table S15 (separate file)

In this file staple oligonucleotide sequences for the brick-like object with staple strand breaking variation E are provided.

Additional Data table S16 (separate file)

In this file staple oligonucleotide sequences for the brick-like object with staple strand breaking variation F are provided.

Additional Data table S17 (separate file)

In this file staple oligonucleotide sequences for the single layer rectangle are provided.

References and Notes

1. B. Alberts *et al.*, *Molecular Biology of the Cell* (Garland Science, New York, ed. 5, 2002).
2. N. C. Seeman, Nanomaterials based on DNA. *Annu. Rev. Biochem.* **79**, 65 (2010).
[doi:10.1146/annurev-biochem-060308-102244](https://doi.org/10.1146/annurev-biochem-060308-102244) [Medline](#)
3. W. M. Shih, J. D. Quispe, G. F. Joyce, A 1.7-kilobase single-stranded DNA that folds into a nanoscale octahedron. *Nature* **427**, 618 (2004). [doi:10.1038/nature02307](https://doi.org/10.1038/nature02307) [Medline](#)
4. P. W. K. Rothemund, Folding DNA to create nanoscale shapes and patterns. *Nature* **440**, 297 (2006). [doi:10.1038/nature04586](https://doi.org/10.1038/nature04586) [Medline](#)
5. S. M. Douglas, J. J. Chou, W. M. Shih, DNA-nanotube-induced alignment of membrane proteins for NMR structure determination. *Proc. Natl. Acad. Sci. U.S.A.* **104**, 6644 (2007). [doi:10.1073/pnas.0700930104](https://doi.org/10.1073/pnas.0700930104) [Medline](#)
6. Y. Ke *et al.*, Scaffolded DNA origami of a DNA tetrahedron molecular container. *Nano Lett.* **9**, 2445 (2009). [doi:10.1021/nl901165f](https://doi.org/10.1021/nl901165f) [Medline](#)
7. E. S. Andersen *et al.*, Self-assembly of a nanoscale DNA box with a controllable lid. *Nature* **459**, 73 (2009). [doi:10.1038/nature07971](https://doi.org/10.1038/nature07971) [Medline](#)
8. S. M. Douglas *et al.*, Self-assembly of DNA into nanoscale three-dimensional shapes. *Nature* **459**, 414 (2009). [doi:10.1038/nature08016](https://doi.org/10.1038/nature08016) [Medline](#)
9. H. Dietz, S. M. Douglas, W. M. Shih, Folding DNA into twisted and curved nanoscale shapes. *Science* **325**, 725 (2009). [doi:10.1126/science.1174251](https://doi.org/10.1126/science.1174251) [Medline](#)
10. Y. Ke *et al.*, Multilayer DNA origami packed on a square lattice. *J. Am. Chem. Soc.* **131**, 15903 (2009). [doi:10.1021/ja906381y](https://doi.org/10.1021/ja906381y) [Medline](#)
11. T. Liedl, B. Höglberg, J. Tytell, D. E. Ingber, W. M. Shih, Self-assembly of three-dimensional prestressed tensegrity structures from DNA. *Nat. Nanotechnol.* **5**, 520 (2010).
[doi:10.1038/nnano.2010.107](https://doi.org/10.1038/nnano.2010.107) [Medline](#)
12. D. Han *et al.*, DNA origami with complex curvatures in three-dimensional space. *Science* **332**, 342 (2011). [doi:10.1126/science.1202998](https://doi.org/10.1126/science.1202998) [Medline](#)
13. Y. Ke, N. V. Voigt, K. V. Gothelf, W. M. Shih, Multilayer DNA origami packed on hexagonal and hybrid lattices. *J. Am. Chem. Soc.* **134**, 1770 (2012).
[doi:10.1021/ja209719k](https://doi.org/10.1021/ja209719k) [Medline](#)
14. B. Wei, M. Dai, P. Yin, Complex shapes self-assembled from single-stranded DNA tiles. *Nature* **485**, 623 (2012). [doi:10.1038/nature11075](https://doi.org/10.1038/nature11075) [Medline](#)
15. S. M. Douglas, I. Bachelet, G. M. Church, A logic-gated nanorobot for targeted transport of molecular payloads. *Science* **335**, 831 (2012). [doi:10.1126/science.1214081](https://doi.org/10.1126/science.1214081) [Medline](#)
16. A. V. Pinheiro, D. Han, W. M. Shih, H. Yan, Challenges and opportunities for structural DNA nanotechnology. *Nat. Nanotechnol.* **6**, 763 (2011). [doi:10.1038/nnano.2011.187](https://doi.org/10.1038/nnano.2011.187) [Medline](#)
17. In the fluorometric experiments, trace amounts of the organic dye SYBR green (SG) were added to one-pot self-assembly reaction mixtures (18). The use of low concentrations of SG corresponding to one SG molecule per ~900 possible DNA base pairs in solution

ensured negligible perturbation of the DNA hybridization processes. The fluorescence brightness of SG is enhanced upon intercalation into dsDNA domains (29); recording the SG fluorescence intensity can thus provide a measure for the evolution of the overall content of DNA base pairs in solution. A specific signal for the formation of object-related DNA base pairs upon incubation for time t at temperature T is obtained by comparison with reference reactions (18). For templated DNA objects—i.e., objects that form by staple DNA strand-assisted folding of a much longer scaffold DNA template molecule (4)—reference reactions were prepared that included the respective set of staple DNA oligonucleotides but lacked the scaffold DNA strand. Cryogenic shock-freezing of a reaction mixture in liquid nitrogen quenched folding and unfolding processes and preserved the state of the reaction at the time and temperature of freezing (18). After quick thawing, the solution content was analyzed using agarose gel electrophoresis and/or direct imaging with negative-stain TEM. Gel electrophoresis and TEM imaging were performed as previously described (30). Excess staple strands were removed by molecular weight cut-off filtration with 100-kD spin filters. Objects were designed using caDNAno (31); models were computed using CanDo (30, 32).

18. Materials and methods are available as supplementary materials on *Science* Online.
19. R. Wei, T. G. Martin, U. Rant, H. Dietz, DNA origami gatekeepers for solid-state nanopores. *Angew. Chem. Int. Ed. Engl.* **51**, 4864 (2012). [doi:10.1002/anie.201200688](https://doi.org/10.1002/anie.201200688) [Medline](#)
20. T. G. Martin, H. Dietz, Magnesium-free self-assembly of multi-layer DNA objects. *Nat. Commun.* **3**, 1103 (2012). [doi:10.1038/ncomms2095](https://doi.org/10.1038/ncomms2095) [Medline](#)
21. M. Ohgushi, A. Wada, “Molten-globule state”: A compact form of globular proteins with mobile side-chains. *FEBS Lett.* **164**, 21 (1983). [doi:10.1016/0014-5793\(83\)80010-6](https://doi.org/10.1016/0014-5793(83)80010-6) [Medline](#)
22. P. L. Privalov, Thermodynamic problems of protein structure. *Annu. Rev. Biophys. Biophys. Chem.* **18**, 47 (1989). [doi:10.1146/annurev.bb.18.060189.000403](https://doi.org/10.1146/annurev.bb.18.060189.000403) [Medline](#)
23. L. L. Porter, G. D. Rose, A thermodynamic definition of protein domains. *Proc. Natl. Acad. Sci. U.S.A.* **109**, 9420 (2012). [doi:10.1073/pnas.1202604109](https://doi.org/10.1073/pnas.1202604109) [Medline](#)
24. R. Jungmann, T. Liedl, T. L. Sobey, W. M. Shih, F. C. Simmel, Isothermal assembly of DNA origami structures using denaturing agents. *J. Am. Chem. Soc.* **130**, 10062 (2008). [doi:10.1021/ja8030196](https://doi.org/10.1021/ja8030196) [Medline](#)
25. G. F. Joyce, Directed evolution of nucleic acid enzymes. *Annu. Rev. Biochem.* **73**, 791 (2004). [doi:10.1146/annurev.biochem.73.011303.073717](https://doi.org/10.1146/annurev.biochem.73.011303.073717) [Medline](#)
26. S. Woo, P. W. K. Rothmund, Programmable molecular recognition based on the geometry of DNA nanostructures. *Nat. Chem.* **3**, 620 (2011). [doi:10.1038/nchem.1070](https://doi.org/10.1038/nchem.1070) [Medline](#)
27. J. Zheng *et al.*, From molecular to macroscopic via the rational design of a self-assembled 3D DNA crystal. *Nature* **461**, 74 (2009). [doi:10.1038/nature08274](https://doi.org/10.1038/nature08274) [Medline](#)
28. W. Liu, H. Zhong, R. Wang, N. C. Seeman, Crystalline two-dimensional DNA-origami arrays. *Angew. Chem. Int. Ed. Engl.* **50**, 264 (2011). [doi:10.1002/anie.201005911](https://doi.org/10.1002/anie.201005911) [Medline](#)

29. H. Zipper, H. Brunner, J. Bernhagen, F. Vitzthum, Investigations on DNA intercalation and surface binding by SYBR Green I, its structure determination and methodological implications. *Nucleic Acids Res.* **32**, e103 (2004). [doi:10.1093/nar/gnh101](https://doi.org/10.1093/nar/gnh101) [Medline](#)
30. C. E. Castro *et al.*, A primer to scaffolded DNA origami. *Nat. Methods* **8**, 221 (2011). [doi:10.1038/nmeth.1570](https://doi.org/10.1038/nmeth.1570) [Medline](#)
31. S. M. Douglas *et al.*, Rapid prototyping of 3D DNA-origami shapes with caDNAno. *Nucleic Acids Res.* **37**, 5001 (2009). [doi:10.1093/nar/gkp436](https://doi.org/10.1093/nar/gkp436) [Medline](#)
32. D. N. Kim, F. Kilchherr, H. Dietz, M. Bathe, Quantitative prediction of 3D solution shape and flexibility of nucleic acid nanostructures. *Nucleic Acids Res.* **40**, 2862 (2012). [doi:10.1093/nar/gkr1173](https://doi.org/10.1093/nar/gkr1173) [Medline](#)